Naval Research Laboratory
Washington, DC 20375-5320

NRL/FR/7130--98-9880

Model Validations and Predictions for Water Barrier Defense

WILLAIM G. SZYMCZAK

Physical Acoustics Branch
Acoustics Division

CHARLES E. HIGDON

Naval Surface Warfare Center
Dahlgren, Virginia

May 12, 1998

REPORT DOCUMENTATION PAGE

Form Approved
OMB No. 0704-0188

1. AGENCY USE ONLY (*Leave Blank*)	2. REPORT DATE	3. REPORT TYPE AND DATES COVERED
	May 12, 1998	Final

4. TITLE AND SUBTITLE

Model Validations and Predictions for Water Barrier Defense

5. FUNDING NUMBERS

PE - 6211N
TA - X01152
WU - 71-M138

6. AUTHOR(S)

William G. Szymczak and Charles E. Higdon*

7. PERFORMING ORGANIZATION NAME(S) AND ADDRESS(ES)

Naval Research Laboratory
Washington, DC 20375-5320

8. PERFORMING ORGANIZATION REPORT NUMBER

NRL/FR/7130--98-9880

9. SPONSORING/MONITORING AGENCY NAME(S) AND ADDRESS(ES)

Office of Naval Research
800 North Quincy Street
Arlington, VA 22217-5660

10. SPONSORING/MONITORING AGENCY REPORT NUMBER

11. SUPPLEMENTARY NOTES

*Naval Surface Warfare Center, Dahlgren, Virginia

12a. DISTRIBUTION/AVAILABILITY STATEMENT

Approved for public release; distribution is unlimited.

12b. DISTRIBUTION CODE

13. ABSTRACT (*Maximum 200 words*)

Validations of a mathematic model and computational code for predicting shallow-depth explosion plume behavior are presented. The model is based on a generalized formulation of hydrodynamics and uses an incompressible liquid assumption. This formulation is well suited for predicting long-time bubble and plume dynamics. Initial conditions for the model are derived from spherically symmetric bubble theory, combined with empirical measurements. The effect of "fingering" of plumes occurring at the center of simultaneously detonated discrete charges in a line is modeled empirically as a recess in the surface due to shock interaction. This model is validated by comparing a three-dimensional (3-D) computation to observations from an experiment. Quantitative measurements of plume heights and plume densities using conductivity probes and microwave absorption are also compared to the computational data using both 2-D line charge and 3-D discrete charge models. Finally, an optimal depth study based on computations of 2-D line charges is presented.

14. SUBJECT TERMS

Underwater explosion bubble
Computational fluid dynamics
Water plumes
Free surface

15. NUMBER OF PAGES

38

16. PRICE CODE

17. SECURITY CLASSIFICATION OF REPORT	18. SECURITY CLASSIFICATION OF THIS PAGE	19. SECURITY CLASSIFICATION OF ABSTRACT	20. LIMITATION OF ABSTRACT
UNCLASSIFIED	UNCLASSIFIED	UNCLASSIFIED	UL

NSN 7540-01-280-550

Standard Form 298 (Rev. 2-89)
Prescribed by ANSI Std 239-18
298-102

CONTENTS

FIGURES

TABLES

MODEL VALIDATIONS AND PREDICTIONS FOR WATER BARRIER DEFENSE

INTRODUCTION

The purpose of this report is to provide both validations and predictions for explosion plume behavior. The experiments presented in this report were conducted in July, 1995, in a water-filled quarry facility in Rustburg, Virginia, operated by Dynamic Testing, Incorporated, a subsidiary of NKF Engineering, Incorporated. The data obtained from these tests are used to validate a computational hydrodynamics model for plume predictions.

Background

This report was prepared in support of the Water Barrier Ship Self Defense Concept, managed by C. E. Higdon of the Naval Surface Warfare Center, Dahlgren Division (NSWCDD), Dahlgren, Virginia, Code G23. Under the sponsorship of the Office of Naval Research (ONR), Arlington, Virginia, the Center is developing technology that has the potential to be very effective in defending Navy platforms against high-speed, low-flying antiship missiles (ASMs). The concept uses a "wall of water" to provide a low-cost, universal terminal defense system for ships. The "wall of water" or "water barrier" is formed from the shallow detonations of multiple underwater explosives to protect the ship from attacking ASMs. This concept can be employed to slow or stop debris and warhead fragments from missiles killed at very short range to preclude significant damage to the defending ship. Furthermore, the barrier would defeat the fusing and structure of ASMs that have penetrated the inner self-defense layer. Further details of this concept may be found in [1].

In a recent work [2], observations of a large set of experiments were used to improve a set of empirical relations for modeling underwater explosion bubbles in an incompressible medium (water). While such relations were derived and reported as long ago as 1948 by Cole [3] these approximations were not valid for very shallow depths due to simplifying assumptions that were made. Using the Rayleigh-Plesset equation for modeling a spherical adiabatic gas bubble oscillating in an infinite incompressible medium, without any simplifying assumptions, together with new measurements of shallow depth explosion bubbles, the new empirical relations provide more accurate initial conditions for hydrodynamics computer codes.

Explosion Dynamics

Upon detonation of an underwater explosive a shock wave moving away from the charge is emitted. This wave reflects off the surface as a rarefaction wave which travels back down through the gas globe of detonation products. Due to the tension created behind the rarefaction wave, a whitened area of cavitation is formed that rises from the surface. Under the surface a bubble is formed from the combustion products, which expands rapidly due to the initially high pressures of its internal gases. The early expansion of the bubble is nearly spherical, after which a water plume forms above the bubble. Eventually, the bubble expands to its maximum volume. If this maximum volume has an equivalent spherical radius that is between approximately one and two times the initial charge depth, a second jet moving downward through the bubble will form during its collapse to a minimum volume. The duration from the time of the detonation to the first collapse is referred to as the "bubble

Manuscript approved January 20, 1998.

period." Since the jet strikes the bottom of the bubble before the minimum volume is attained, the bubble forms an annular region. As the annular bubble re-expands, secondary plumes are ejected radially, surrounding the central initial plume.

In the case of a line charge or several point charges placed sufficiently close together, a cylindrical bubble is formed. The initial plume forms a wall of water above the line of charges. Secondary plumes erupt on either side of the central plume after the first bubble collapse.

The shock related phenomena described above typically occurs on the order of a millisecond or less. For the examples discussed in this report, bubble periods are approximately 0.6 s with secondary plumes erupting shortly afterward. The entire duration, from the detonation to the plume falling back down to the water surface, usually lasts between 4 and 6 seconds.

Model Approach

The computer codes used for the simulations and modeling presented in this report are based on a generalized formulation of hydrodynamics [2,4-10]. This method is well suited for the study of shallow-depth explosion plumes for the following reasons:

1. The "water" or "liquid" region is modeled as incompressible, thereby allowing for time steps proportional to the inverse of the water velocity as opposed to the much smaller time steps that a compressible formulation would require based on the speed of sound in water. This is important because plume behavior occurs on the order of seconds.

2. The model allows for regions of "spray," which is typical of plume behavior in which a well defined interface between the bubble and water or especially the water and the air does not exist.

3. The computational model uses a fixed "Eulerian" grid providing for generality in studying complex bubble dynamics and free surface topology changes. For shallow-depth explosions this includes the underwater bubble forming one or more annular regions as a downward moving jet intersects the bottom surface of the bubble as it collapses, in addition to the radial plumes ejected on the bubble's second expansion, and the eventual venting of the bubble into the atmosphere.

Our approach has some similarities to the volume of fluid (VOF) approach developed by Hirt and Nichols [11] and, more recently, by Kothe and Mjolsness [12]. Our method differs in some important ways from these typical VOF methods. First, the theory behind the model was designed specifically for violent surface motions characterized by collisions of different portions of the free surface. In particular, when collisions occur, the VOF variable will often attain a value larger than one (due to numerical error or fluid elements running into each other). When this occurs, VOF formulations simply truncate the overage. This process violates conservation of mass and can introduce small instabilities by increasing the total energy of the solution. Using the generalized formulation, density is redistributed in such a way that the total mass is conserved and the momentum is redistributed so that the energy is nonincreasing (but may decrease when liquid collisions occur). This method solves conservation of mass and momentum equations, which are subject to density and pressure (when cavitation is an issue) constraints. The density constraint, together with the conservation of mass equation, are equivalent to the usual divergence free constraint for incompressible flow in regions where the density is at its maximum (liquid) value. These equations are solved numerically using a split step procedure. First, the conservation equations are approximated without regard to the constraints using a second order Godunov Method with monotonized slope limiting, as described in [13]. Next, the density constraint is imposed through the

solution of a variational inequality, which becomes a linear complimentarity problem upon discretization. Finally, the pressure is determined using a projection method discretized using a finite element method. This algorithm has been implemented for both a two-dimensional (2-D) (or axially symmetric) code BUB2D [2,4-7,9], and a three-dimensional (3-D) code in generalized coordinates BUB3D [8-10].

THE COMPUTATIONAL MODEL

Model Equations

The computational model used for both the 2- and 3-D codes is based on a generalized formulation of hydrodynamics. This formulation uses a fixed spatial domain Ω, where the density ρ, velocity $\mathbf{u}$, and the pressure p are governed by the mass and momentum conservation equations

$$\rho_t + \nabla \bullet (\rho \mathbf{u}) = 0 \tag{1}$$

$$(\rho \mathbf{u})_t + \nabla \bullet (\rho \mathbf{u}\mathbf{u}) = -\rho g \mathbf{k} - \nabla p \tag{2}$$

subject to the constraint

$$\rho \le \rho_0, \tag{3}$$

where ρ_0 is the constant density of the incompressible liquid. In (2) $-\mathbf{k}$ is the unit vector in the direction of the gravitational force, and g is the gravitational constant. In regions where $\rho = \rho_0$, Eq. (1) becomes the usual divergence free condition for incompressible flow. We define the time varying "liquid" domain $\mathbf{D}(t)$ by

$$\mathbf{D}(t) = \{\mathbf{x} : \rho(\mathbf{x},t) = \rho_0\}. \tag{4}$$

The non-liquid domain is defined using

$$\Omega - \mathbf{D}(t) = \mathbf{A}(t) \cup \mathbf{B}(t) \cup \mathbf{C}(t), \tag{5}$$

where the regions **A**, **B**, and **C** are disjoint. Within these regions, the pressure is assumed to be uniform; that is

$$p(\mathbf{x},t) = \begin{cases} p_A & \mathbf{x} \in \mathbf{A}(t) \\ p_B(t) & \mathbf{x} \in \mathbf{B}(t) \\ p_C & \mathbf{x} \in \mathbf{C}(t) \end{cases}. \tag{6}$$

In the above, p_A represents the constant ambient "air" pressure. The "bubble" pressure, $p_B(t)$, is usually determined using an adiabatic gas assumption

$$p_B(t) = c(V_B(t))^{\gamma}; \tag{7}$$

where c is constant, γ is the (constant) ratio of specific heats of the bubble gases, and $V_B(t)$ is the bubble volume, which can be determined using

$$V_B(t) = \int_{\mathbf{B}(t)} \left(1 - \frac{\rho(\mathbf{x},t)}{\rho_0}\right) dx. \tag{8}$$

Finally, p_C is the "cavitation" pressure, which is usually set to the vapor pressure of the liquid at some specified temperature. When cavitation is to be modeled, an additional constraint is imposed on the pressure, namely that $p(\mathbf{x},t) \geq p_C$ (see [8]). For the results presented here, this constraint was not imposed, that is, $p_C = -\infty$.

Numerical Algorithm

Assume that the density and velocity, $\rho^n, \mathbf{u}^n$ at time step n are known together with the pressure gradient at the previous half step, $\nabla p^{n-1/2}$. This solution is evolved from time $t = t^n \rightarrow t^n + \tau \equiv t^{n+1}$ using the following three step time split procedure.

Convection

The solution is first advanced $\left(\rho^n, \mathbf{u}^n\right) \rightarrow \left(\tilde{\rho}, \tilde{\mathbf{u}}\right)$ by "solving" the conservation laws (1-2) without including the term ∇p on the right-hand side of Eq. (2) and without regard to the constraint Eq. (3). This step is fully discretized using a formally second-order Godunov-type method, which uses slope limiting in space and explicit predictor-corrector time stepping (e.g., [13]). Although the pressure gradient is not explicitly added to the momentum here, it is used within the predictor step of the Godunov method. Further details of this step may be found in Refs. 4 and 6 for axially symmetric flow problems.

Redistribution of Density and Momenta

Next, the density and momenta are redistributed $\left(\tilde{\rho}, \tilde{\mathbf{u}}\right) \rightarrow \left(\bar{\rho}, \bar{\mathbf{u}}\right)$ so that the constraint Eq. (3) is satisfied, the global conservation of mass and momenta are maintained, and the energy is nonincreasing. The density is redistributed using an approximate solution to the obstacle problem

$$\nabla^2 H = \begin{cases} \rho_0 - \tilde{\rho} & \text{if} \quad H > 0 \\ 0 & \text{if} \quad H = 0 \end{cases}, \tag{9a}$$

and setting

$$\bar{\rho} = \tilde{\rho} + \nabla^2 H. \tag{9b}$$

These equations have been derived by considering a Boltzmann formulation for modeling inelastic fluid collisions and are discussed in greater detail in Refs. 4, 6, and 9. These references also contain details of the numerical discretization of Eq. (9) and the solution procedure, which employs a constrained direction preconditioned conjugate gradient method. The momenta redistributions are determined as solutions of two (or three for 3-D problems) elliptic self-adjoint problems

$$\overline{\rho \mathbf{u}} = \tilde{\rho}\tilde{\mathbf{u}} + \nabla^2\left(H\bar{\mathbf{u}}\right). \tag{10}$$

Discretizations of Eq. (10) yield systems of linear equations with diagonally dominant matrices, which are efficiently solved using a diagonally preconditioned conjugate gradient method. The importance of this step to the overall accuracy and stability of the algorithm was discussed in Ref. 7.

As mentioned in the introduction, this redistribution step is a major distinguishing feature between this algorithm and other VOF approaches (e.g., [11,12]) which would simply truncate the density values.

Multiple Bubbles and Venting

After the redistribution, $\bar{\rho} = \rho^{n+1}$, and the new nonliquid regions are then determined along with the pressure in each of its connected subsets. In the computational space, the new liquid region, $\mathbf{D}^{n+1} = \mathbf{D}(t^{n+1})$, is defined to be the collection of grid cells C_l such that

$$\rho_l^{n+1} \geq (1-\varepsilon_\rho)\rho_0, \tag{11}$$

where ρ_l^{n+1} is the density in cell C_l. For shallow-depth explosion bubbles, the choice of ε_ρ is important. In general, small values of ε_ρ will cause cells with only slightly less density than the liquid to be treated as regions with uniform pressure, while larger values will cause more of the "spray" (where $0 < \rho < \rho_0$) to be treated as a variable density incompressible region.

In addition to the distinction in the nonliquid regions designated by "air" **A**, "bubble" **B**, and "cavitation" **C**, each component (connected disjoint subset) of **B** is also accounted for. That is, suppose

$$\mathbf{B}^n = \bigcup_{k=1}^{K^n} B_k^n,$$

where K^n is the number of distinct bubbles at time step n, and B_k^n is the component corresponding to bubble k at time step n. When the bubble components B_k^n remain distinct, their pressures p_k^n behave adiabatically

$$p_k^n = c_k (V_k^n)^\gamma,$$

where V_k^n represents the volume of B_k^n, and c_k is constant for all steps n for which the component has no interactions. If a bubble component splits into two distinct regions, say, $B_k^n \to B_l^{n+1} \cup B_m^{n+1}$, the new pressures p_l^{n+1} and p_m^{n+1} are computed assuming the volume changes occurred before the split; that is,

$$p_l^{n+1} = p_m^{n+1} = \frac{p_k^n (V_k^n)^\gamma}{(V_l^{n+1} + V_m^{n+1})^\gamma}.$$

Similarly, if two distinct bubbles merge into a single component region, for example, $B_l^n \cup B_m^n \to B_k^{n+1}$, the new pressure is given by

$$p_k^{n+1} = \frac{(p_l^n V_l^n + p_m^n V_m^n)(V_l^n + V_m^n)^{\gamma-1}}{(V_k^{n+1})^\gamma}.$$

These formulas have been extended to the general case treating any finite number of bubbles merging and splitting in [5]. Whenever merging occurs, the pressure of the new component changes instantaneously. Similarly, when a bubble comes in contact with the air region (that is a cell in B_k^n is

adjacent to a cell in **A**), the bubble is said to "vent" into the air with the pressure instantaneously changing to the air pressure. This is obviously a crude approximation to the finite amount of time the venting would actually take or to the partial venting of the bubble. In particular, if the relatively thin layer of water between the bubble and air is under-resolved by the computational grid, the computed bubble may vent prematurely causing gross errors in the subsequently computed dynamics. In order to prevent this premature venting, the value of ε_ρ in (11) is allowed to depend upon both time and space by the prescription

$$\varepsilon_\rho = \varepsilon_l^n = \begin{cases} \varepsilon_A & C_l \in \mathbf{N}(\mathbf{A}^n) \\ \varepsilon_B & otherwise \end{cases}, \tag{12}$$

where $\mathbf{N}(\mathbf{A}^n)$ is the set of cells that are either in or adjacent to the time varying domain $\mathbf{A}^n$.

Consider the case where $\rho_l^n \geq \left(1-\varepsilon_l^{n-1}\right)\rho_0$ so that $C_l \in \mathbf{D}^n$ but, on the next step, the density decreases below the liquid cutoff, that is, $\rho_l^{n+1} < \left(1-\varepsilon_l^n\right)\rho_0$. If there is a cell in the neighborhood that was nonliquid ($C_k \in \mathbf{N}(C_l) \cap \left(\mathbf{A}^n \cup \mathbf{B}^n \cup \mathbf{C}^n\right)$) then cell C_l would be merged into the nonliquid component containing that cell. If there are more than one nonliquid components in the neighborhood, these components are merged together. However, the case when there are no nonliquid neighboring cells is more problematic. Since the velocity filed in the liquid is divergence free, the density can decrease only because of numerical error. Previously this case was treated by resetting $\rho_l^{n+1} = \left(1-\varepsilon_l^n\right)\rho_0$ so that the cell remained a liquid cell. However, this obviously adds mass, and violates the conservation law. Furthermore, this added mass can be large in the special case when $\varepsilon_l^{n-1} = \varepsilon_A$, but $\varepsilon_l^n = \varepsilon_B$. Even without a decrease in density, the added mass in this case would be $\left(\varepsilon_A - \varepsilon_B\right)\rho_0 |C_l|$, where $|C_l|$ is the volume of C_l. In order to avoid these potentially large errors in added mass, the density is no longer modified in this case. Instead, the cell remains part of the liquid domain, $C_l \in \mathbf{D}^{n+1}$. Thus, the liquid domain is now defined as the collection of cells C_l such that either Eq. (11) holds or $\mathbf{N}(C_l) \subset \mathbf{D}^n$. That is:

$$\mathbf{D}^{n+1} = \bigcup_l C_l : \rho_l^{n+1} \geq \left(1-\varepsilon_\rho\right)\rho_0 \text{ or } \mathbf{N}(C_l) \subset \mathbf{D}^n. \tag{13}$$

Pressure Projection

In the nonliquid region $\bar{\mathbf{u}} = \mathbf{u}^{n+1}$. However, $\bar{\mathbf{u}}$ is not consistent with Eq. (2) in the new liquid region. In this region the velocity is corrected, $\bar{\mathbf{u}} \to \mathbf{u}^{n+1}$, using the gradient of the new pressure, $\nabla p^{n+1/2}$. The pressure $p^{n+1/2}$ is the solution of

$$\tau \nabla \bullet \left(\frac{\nabla p}{\rho^{n+1}}\right) = \nabla \bullet \bar{\mathbf{u}} \quad \text{in } \mathbf{D}^{n+1}. \tag{14}$$

The new velocity, given by

$$\mathbf{u}^{n+1} = \bar{\mathbf{u}} - \tau \frac{\nabla p^{n+1/2}}{\rho^{n+1}} \tag{15}$$

is divergence free in $\mathbf{D}^{n+1}$ and, thus, is consistent with Eq. (1). Equations (14) and (15) define a projection $\mathbf{u}^{n+1} = P(\bar{\mathbf{u}})$ onto the space of divergence free velocities. This equation is discretized using a finite element method with bilinear (in 2-D) or trilinear (in 3-D) elements. This spatial discretization produces an approximate projection which has been analyzed in Ref. 14. The resulting linear system from the discretization of Eq. (14) is solved using an incomplete Cholesky preconditioned conjugate gradient method.

To determine the pressure uniquely using Eq. (14), boundary conditions must be specified. On those portions of the boundary of $\mathbf{D}^{n+1}$ that correspond to "wall" boundaries of Ω, a Neumann condition is specified, namely

$$\frac{\partial p}{\partial \mathbf{n}} = \frac{\rho^{n+1}}{\tau} \bar{\mathbf{u}} \bullet \mathbf{n}. \tag{16}$$

Note that this condition, together with Eq. (15), implies that $\mathbf{u}^{n+1} \bullet \mathbf{n} = 0$ along wall boundaries. Since the pressure is assumed to be continuous, Dirichlet conditions for the pressure along the nonliquid regions are determined according to Eq. (6). In particular, we specify

$$p(\mathbf{x},t) = \begin{cases} p_A & \mathbf{x} \in \partial\mathbf{A}^{n+1} \cap \partial\mathbf{D}^{n+1} \\ p_B^{n+1} & \mathbf{x} \in \partial\mathbf{B}^{n+1} \cap \partial\mathbf{D}^{n+1} \\ p_C & \mathbf{x} \in \partial\mathbf{C}^{n+1} \cap \partial\mathbf{D}^{n+1} \end{cases} \tag{17}$$

along those boundaries common to the nonliquid regions. Hydrostatic pressure Dirichlet conditions are set on other portions of the boundary of Ω to model "cutoff" boundaries.

Initial Conditions

For a single charge, the bubble is initialized as a spherical "void," with zero density, radius A^0, and pressure p_B^0, surrounded by a liquid region at rest. In the case of a line charge or a series of single charges placed sufficiently close in a straight line, the bubble is initialized as a circular cylinder of infinite length. The initial values for the bubble radius and pressure depend on the hydrostatic pressure at the depth of the charge, the charge weight, and empirical constants which depend on the charge type, derived from considering the equation of motion of a spherical bubble in an infinite incompressible medium. In this case, the bubble remains spherical, and its radius oscillates periodically between its minimum, A_{min}, and maximum, A_{max}, values.

Empirical Relations

The following empirical relations are valid for shallow-depth underwater explosions (see Ref. 2)

$$A_{min} = qW^{1/3} \tag{18}$$

$$P_\infty = d + p_A \tag{19}$$

$$G(\alpha) \equiv \frac{1}{\alpha}\left(\frac{1-\alpha^{3(1-\gamma)}}{1-\alpha^{-3\gamma}}\right)^{1/3} = \frac{q}{J_\infty} P_\infty^{1/3} \tag{20}$$

$$p_B^0 = P_\infty(1-\gamma)\left(\frac{1-\alpha^3}{1-\alpha^{3(1-\gamma)}}\right). \tag{21}$$

In the equations listed above, q is the empirical *minimum radius constant,* which depends on the charge type; W is the charge mass; d is the initial charge depth; and p_A is the ambient air pressure. If d is measured in units of feet and p_A in feet of water, then P_∞ is the hydrostatic pressure at the charge depth in units of feet of water. In Eq. (20), γ is the ratio of specific heats for the bubble gases, and J_∞ is the empirical *maximum radius constant.* In the above equations, the value for α must be determined as the solution to Eq. (20) with a given value for the right-hand side. This can be done approximately using Newton's method. The value α is also the ratio of maximum to minimum bubble radii,

$$\alpha = \frac{A_{max}}{A_{min}}, \tag{22}$$

so that

$$A_{max} = J_\infty\left(\frac{1-\alpha^{3(1-\gamma)}}{1-\alpha^{-3\gamma}}\right)^{1/3}\frac{W^{1/3}}{P_\infty^{\,1/3}} \equiv J_\alpha\frac{W^{1/3}}{P_\infty^{\,1/3}}. \tag{23}$$

In cases when the depth ranges between 100 and 1000 ft, it was noted in Ref. 3 that values for J_α remain nearly constant. Because of this and the interest in the relatively deeper charge depths, subsequent reports (e.g., [15,16]) used Eq. (23) under this assumption. However, J_α depends on α, which can change significantly, particularly at shallow depths. This dependence was studied in detail in Ref. 2.

For line charges approximated as a circular cylinder of infinite extent, the corresponding formulas were derived in Ref. 2.

$$A_{min}^{(2D)} = q^{(2D)}M^{1/2} \tag{24}$$

$$q^{(2D)} = \frac{2}{\sqrt{3}}q^{3/2} \tag{25}$$

$$\alpha^{(2D)} = \alpha^{3/2} \tag{26}$$

$$J_\infty^{(2D)} = \frac{2}{\sqrt{3}}J_\infty^{\,3/2} \tag{27}$$

$$A_{\max}^{(2D)} = J_\infty^{(2D)}\left(\frac{1-(\alpha^{(2D)})^{2(1-\gamma)}}{1-(\alpha^{(2D)})^{-2\gamma}}\right)^{1/2}\frac{M^{1/2}}{P_\infty^{\,1/2}}. \tag{28}$$

In Eqs. (24) and (28), M is the mass per unit length.

For the tests considered in this study, all charges were Composition C-4. Based on our previous analysis (Ref. 2, Table 3-7), the values used in this study are $\gamma = 1.34$, $q = 0.286$, and $J_\infty = 15.3$.

Shock Effects

It was noted by Kedrinskii in Ref. 17 that using an incompressible liquid model for shallow-depth explosion simulations generally underpredicts the plume heights for early times. It has been demonstrated in Refs. 2 and 17, that an indentation of the free surface directly above the charge will increase the plume heights predicted by an incompressible liquid model. This indentation represents the effects of spalling from the reflection of the detonation shock wave from the surface. In addition to this reflection, shock interaction from the simultaneous detonation of multiple charges has been shown to cause plume fingering between the initial charge locations. An empirical model for this phenomenon is shown in Fig. 1.

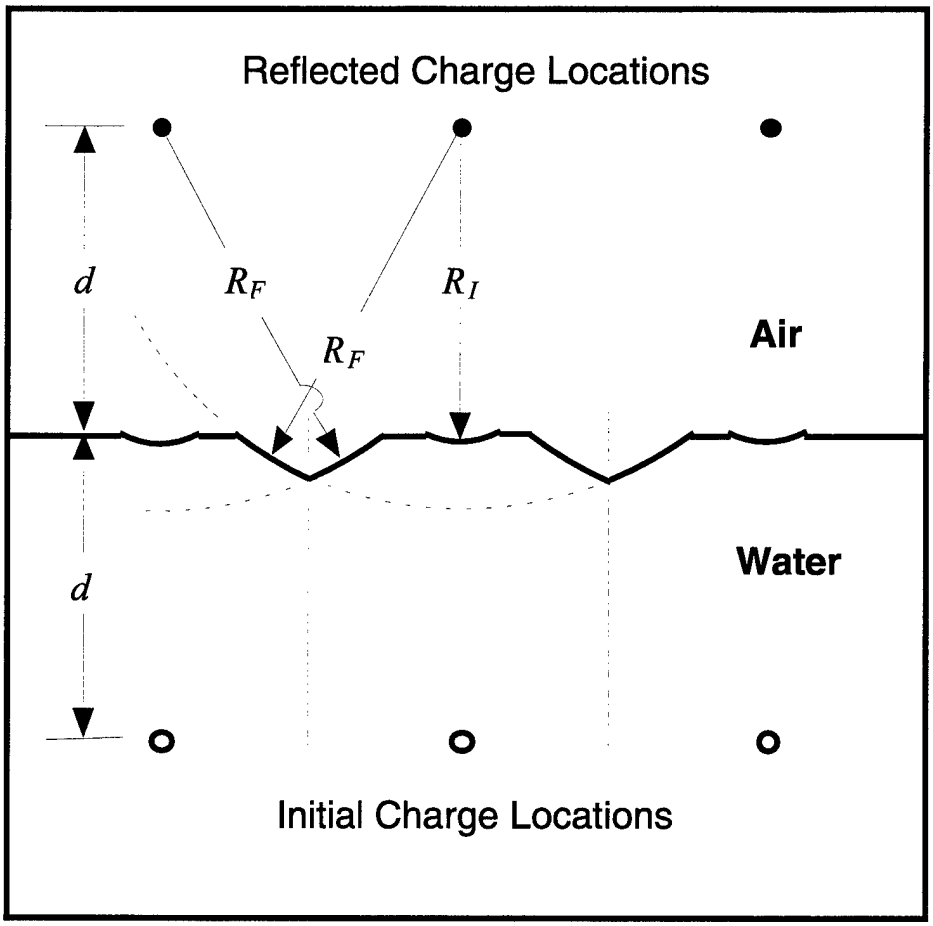

Fig. 1 — Empirical model for shock effects

NUMERICAL RESULTS AND VALIDATIONS

In this chapter, validations of the 2-D computational model are first presented. Comparisons of the computations to experimental data include plume height measurements from video cameras images and plume density measurements from both conductivity probes and microwave absorption. The computational model is then used to determine an "optimal depth study" in which a measure of

the plume density as a function of charge depth is maximized. Finally, the empirical shock model displayed in Fig. 1 is validated using the BUB3D code.

The tests described here were conducted in a 130-foot-deep water-filled quarry operated by Dynamic Testing, Incorporated (DTI) in Rustburg, Virginia, during July 1995. The charges used in the experiments were configured in a line comprised of five to eight discrete 10-lb blocks of C-4 separated by 8 ft or as a continuous line charge of length 40 ft to 56 ft. A more detailed description of these tests has appeared in Ref. 18. The subset of tests considered here are summarized in Table 1. In this table, N is the number of discrete charges in the configurations, S is the distance between the center of the charges, $A_{max}^{(2D)}$ is the maximum theoretical radius of the cylindrical bubble as determined using Eq. (28), and C is the scaled depth, $C = d / A_{max}^{(2D)}$. The parentheses surrounding the number of charges of the continuous type indicate that these were actually comprised of individual 1-lb blocks of C-4 in a line.

Table 1 — Test Shot Descriptions

Shot No.	Type	d (ft)	N	S (ft)	M (lb/ft)	$A_{max}^{(2D)}$ (ft)	C
2	Discrete	8.2	5	8	1.25	11.53	0.71
6	Discrete	8.2	8	8	1.25	11.53	0.71
7	Continuous	8.2	(56)	(1)	1.25	11.53	0.71
9	Discrete	8.2	5	8	1.25	11.53	0.71
10	Discrete	9.4	5	8	1.25	11.36	0.83
11	Continuous	9.4	(40)	(1)	1.25	11.36	0.83

Validations of the Two-Dimensional Model

The two-dimensional (2-D) model uses an initial approximation of the bubble as a circular cylinder of infinite extent. This approximation is reasonable for the discrete tests only if the distance between charges is relatively small when compared to the maximum diameter of the spherical bubble from an individual charge. For the discrete tests listed in Table 1, the individual 10-pound charges of C-4 would generate bubbles with maximum radii $A_{max} = 9.3$, when $d = 8.2$, and $A_{max} = 9.2$ at $d = 9.4$. Since these values are greater than the charge standoff of 8 ft, it can be expected that the bubble dynamics will be adequately represented by the 2-D approximation. However, it can be expected that shot numbers 7 and 11 will be better represented by this approximation.

The grids used in this study are tensor product grids. That is, the grid point locations may be defined as a tensor product of two one-dimensional (1-D) grids. Typically, the grids are constructed with uniform spacing in both directions in the vicinity of the bubble, with grid stretching to approximate either conditions at infinity or a wall boundary relatively far away. The x-direction is taken to be the horizontal line perpendicular to the line charge (cylindrical axis). For single line charges, $x = 0$ is a symmetry plane. The z coordinate measures vertical displacement with the convention that $z = 0$ corresponds to the initial location of the water-air interface.

Cylindrical explosion bubbles are more difficult to resolve numerically than axially symmetric bubbles due to the greater values of the radius ratio $\alpha^{(2D)}$. For the test shots in Table 1, the initial

(minimum) bubble radius (determined using Eq. (24)) is $A_{min}^{(2D)} = 0.197$ so that $\alpha^{(2D)} > 57$. Thus, the use of a single uniform grid capable of resolving the initial bubble and extending beyond the bubble at its maximum size would contain a prohibitively large number of cells. One method of alleviating this problem is through the use of two separate grids.

The 2-D solutions were computed in two steps. Initially, a grid that was fine in a region surrounding the charge line was used until the bubble approached the boundary of the fine region. Then the solution was remapped, conserving mass and momentum onto a grid that was coarser than the fine grid region of the first grid but still able to resolve the bubble after the initial grid had been used. This second grid was uniform in a large enough region to contain the important long-time dynamics of the problem. For example, the initial grid used in these computations consisted of 40×100 square cells of size $h_1 = 0.05$ in the region $0 \le x \le 2$ intersected with $-d-2.5 \le z \le -d+2.5$. Outside of the uniform region, cells were stretched horizontally to $x = X_r = 110$ and downward to $z = Z_b = -115$ using 40 additional grid lines in each direction. Above the uniform region, the spacing in the z direction was uniformly set to $\Delta z = 0.1$ in the region $-d+2.5 \le z \le 2$. The initial grid was used for $0 \le t \le t_i = 0.007$, while the cylindrical bubble grew from its initial radius of 0.197 to approximately 1.6. The computed solution at $t = t_i$ was then remapped onto the second grid.

The numerical errors were approximated by using two different grids for the second step of the computations. Each grid contained square cells of size h_2 in the region $0 \le x \le 12$ intersected with $-d-11 \le z \le 28$. As with the initial grid domain, the second grids were stretched horizontally to $x = X_r = 110$ and downward to $z = Z_b = -115$. To simulate the tests where the initial charge was at depth $d = 8.2$, the grids were stretched upward to $z = Z_t = 180$ and, in the case when $d = 9.4$, they were stretched to $z = Z_t = 125$. The "fine" grids contained a uniform region with $h_2 = 0.2$ and used a total of 100×305 cells, and the "coarse" grids contained a uniform region with $h_2 = 0.4$ and used a total of 50×160 cells.

The effect of using an indented channel in the surface above the line of charges was also tested. This was done by performing the computations using both an initially "flat" and "indented" free surface. The indentations are determined using the model shown in Fig. 1 with $R_I = 1.03d$, which is the same value used in Ref. 2 for axially symmetric computations with a single charge.

A summary of the runs with computed bubble periods, T_h (the computed time that the bubble attains its minimum radius) and maximum radii, $A_{max,h}^{(2D)}$, is listed in Table 2. Here, the radius refers to the equivalent radius of a cylinder with the same cross-sectional area since the bubbles will in general not remain circular. The number of time steps taken to the first bubble minimum, $N(T_h)$, and the total number of steps, $N(T_F)$, to reach the final time $T_F = 6.0$, are also listed. The time steps for the runs were adaptively selected, based on changes in equivalent radius. The number of steps taken until the first bubble minimum is determined by an input tolerance, which was halved for the fine grid runs. The execution times in Table 2 are in minutes on a Silicon Graphics Impact 2 workstation with an R10000 processor, compiled using *f77 -O3 -mips4 -n32 -r10000*. The times listed are for the completion of the second step of the run only. The execution time for the initial grid was approximately 15 min.

Table 2 — Run Summary

Run	d	Surface	Second Grid	$A_{max,h}^{(2D)}$	T_h	$N(T_h)$	$N(T_F)$	Execution time
7-C	8.2	flat	coarse	10.824	0.5921	466	1912	28.1
7-CI	8.2	indented	coarse	10.761	0.5898	448	1978	29.5
7-F	8.2	flat	fine	10.903	0.5862	860	3574	409.1
7-FI	8.2	indented	fine	10.820	0.5859	874	3605	407.1
11-C	9.4	flat	coarse	10.787	0.6087	463	1927	28.4
11-CI	9.4	indented	coarse	10.753	0.6069	465	1955	28.7
11-F	9.4	flat	fine	10.880	0.6034	876	3826	402.4
11-FI	9.4	indented	fine	10.840	0.6019	884	3761	415.8

The values of $A_{max,h}^{(2D)}$ listed in Table 2 indicate that the depth has little influence on the maximum radius. However, the fine grid values are approximately 1% greater than the coarse grid values. Since the grid sizes and time steps were approximately halved in the fine grid and first order convergence has been observed for the maximum radius (and period) using this numerical method, the difference in the two solutions provides an estimate of the numerical error. The computed periods at the shallower depth are consistently shorter than at the greater depth. This is consistent with the theoretical and experimental observations reported in Ref. 2 due to the proximity of the free surface. As with the maximum radius values, the periods computed using the fine grids are approximately 1% greater than on the corresponding coarse grid

Plume Observations

Density contours of the plumes at $t = 0.2$, 0.5, 1.0, and 2.5 for the computational Runs 7-C, 7-F, 7-CI, and 7-FI are displayed in Fig. 2. These images are based on a shading corresponding to the logarithm of the density. This enables the relatively low density of the spray in the plume to be easily observed. Densities less than 0.1% of the water density are represented as a "white" region, and "black" corresponds to the water density.

At time $t = 0.2$, the "egg-shaped" bubble has nearly attained its maximum radius. The bubble profiles for the four cases at this time are nearly indistinguishable, except for the slightly irregular profile of the bubble in Run 7-C. A small region of "numerical spray" has begun to form above the water on top of the bubble. This corresponds to the "Rayleigh-Taylor" instability at the water-air surface, where the water has an upward velocity but is being accelerated downward due to the below ambient pressure inside the bubble. Further discussions of instabilities due to explosion bubble dynamics are included in Refs. 4 and 9. A small thin upward moving water jet has formed in the cases when the initial surface was indented. This phenomenon has been described in Ref. 17 and examined further in Ref. 2.

At time $t = 0.5$, the bubble has begun to collapse. During this collapse a high-pressure stagnation point forms in the water above the bubble. This in turn causes the formation of a "double jet"; a small one moving downward through the bubble, and a larger one forming the central water column of the plume. Similar jetting behavior has been observed for axially symmetric bubbles by Blake and Gibson in Ref. 19. In the computations, this central column is surrounded by the numerical spray region, which is moving upward but is being accelerated downward by gravity. The thin jet caused by the indentation rises approximately 10 ft above the numerical spray. Once again, there is little difference between the bubble and plume profiles for the coarse and fine grid run comparisons.

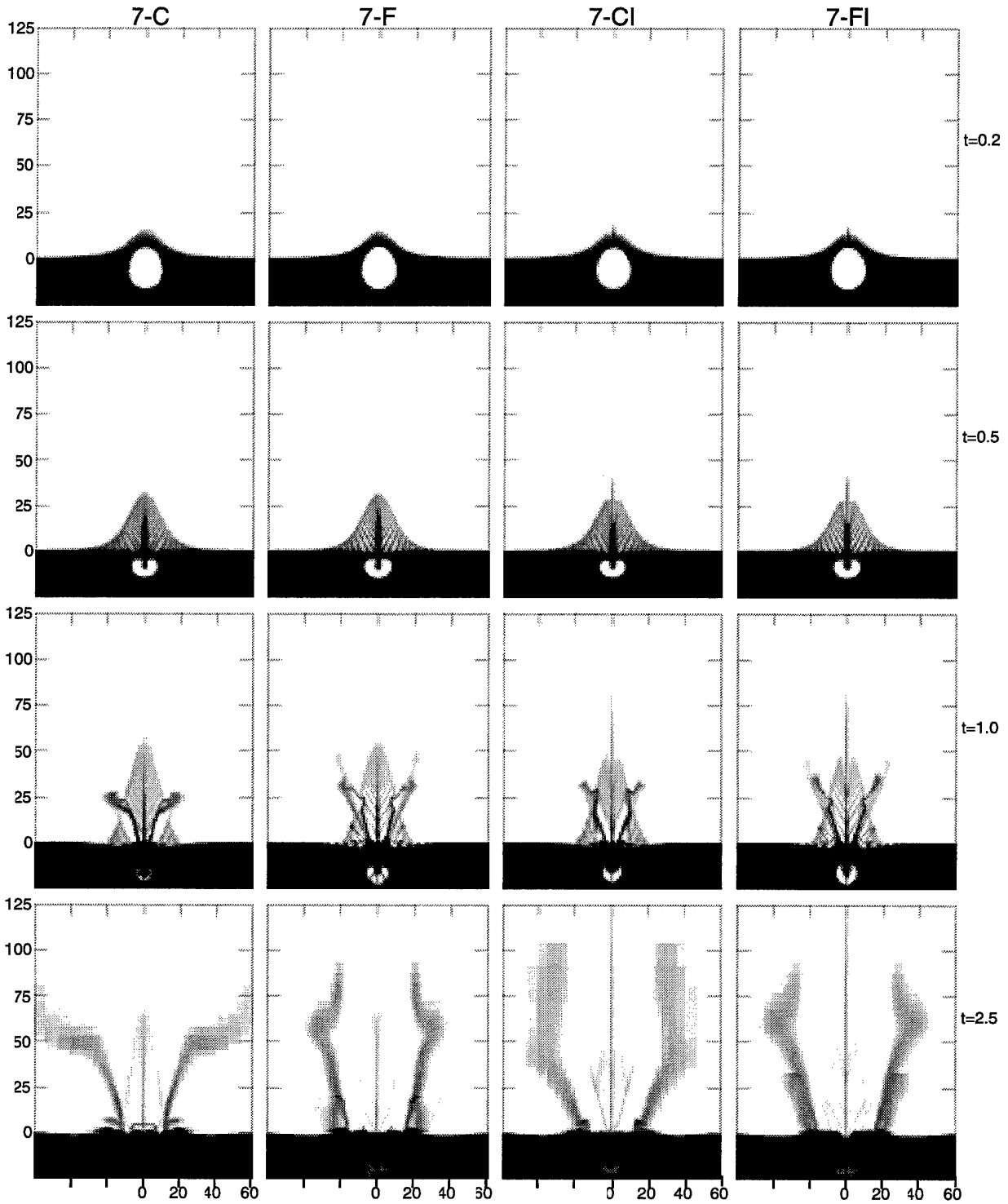

Fig. 2 — Computational runs for Shot 7

As indicated in Table 2, the bubble period for all four runs was approximately 0.59 s. As the bubble re-expands, secondary plumes are ejected upward and outward on the sides of the central plume. At time $t = 1.0$, the bubble has begun its second contraction, and the secondary plumes have

reached a height of over 25 ft, and a total width of over 40 ft. At this time, differences in the details inside the plume structure become more evident at the different grid resolutions. On the fine grid runs, the plume structures are almost identical, except for the thin central plume, which remains higher in the indented surface case. The top of the secondary plume from Run 7-C is slightly wider and lower than with Run 7-CI. Differences in the solutions as time progresses are expected due to the water-air instabilities mentioned above and the instabilities at the bubble interface near bubble minimums. However, the overall qualitative behavior of the plume and bubble appears to be reproducible.

Plume differences are more apparent at $t = 2.5$. At this time, the plumes have begun falling downward with gravity, and the bubble has little remaining energy. Bubble energy is reduced in our computational model through both numerical dissipation and through our redistribution step and treatment of liquid-on-liquid collisions. For further discussions on energy losses, see Refs. 4, 6, 7, and 9. The widths and heights of the secondary plumes for the coarse grid runs have continued to diverge. In the indented runs, the plume structure is similar between the two grids, with the coarse grid secondary plume extending higher (probably due to the use of the stretched grid cells). Some detail in the plume structure at a height of about 30 ft appears in the fine grid Run 7-FI due to one of the bubble pulsations. During the computations, the bubble typically underwent ten pulsations before venting at about $t = 4.5$. This plume detail can also be seen at a height of about 20 ft in Run 7-F and just above the surface for the coarse grid runs. Comparing the four runs demonstrates that the major difference between using the flat or indented surface is the height of the thin central plume, and even though some detail is lost with the coarse grids, their solutions agree qualitatively with the finer grid runs, particularly at the early times.

Figure 3 displays graphs of the computed plume heights as a function of time for DTI Shot 7. Here, the plume height was defined as the highest location of a grid cell having a density greater than 1% of the water density. When the free surface has an initial indentation the primary central plume always remains higher than the secondary plumes, as indicated by the smooth nearly parabolic profiles from Runs 7-CI and 7-FI. In this case the difference between the fine and coarse grids is relatively small. For the first second the relative error is less than 3%. The error increases to about 6% at $t = 2$ s, and the error in the maximum computed plume height is under 8%. The inflection point in the plume height for Run 7-F shortly after $t = 1.1$ was caused by the secondary plume rising above the central plume. In Fig. 2 the details of this secondary plume, and of subsequently ejected plumes are not reproduced on the coarse grid Run 7-C. The discontinuity in the plume height at $t = 3.5$ s for Run 7-F occurs as the density of the falling plume decreases below 1% of the water density. This happens because the plume has a horizontal velocity and becomes under-resolved (diffused) as it passes through the stretched cells in the grid.

Figure 4 displays the computed plume heights for Shot 11. The plume heights are roughly 25% lower than the computed results for Shot 7. As before the agreement between the coarse and fine grid results with the initially indented free surface (Runs 11-CI and 11-FI) is very good, except for $t > 3$, when part of the coarse grid secondary plume extends above the primary plume.

Measurements of the plume heights using video frames were documented in Ref. 18. The measured heights for Shot 7 are compared to the results from the fine grid computations in Fig. 5. After $t = 1.2$ s, plume height measurements were not possible due to a combination of the poor definition of the top of the plume and low contrast. While the computations using a flat initial surface under predict the measurements by over 30%, the use of the initial indentation produces relative errors under 10%. At early times the higher values for the measured heights are conjectured to be caused by the initial shock spalling water from the surface. Recall, we are not modeling the

shock directly, but only empirically using the indentation above the surface. At later times, the computed heights for Run 11-FI overtake the measurements. This is very likely due to drag on the top of the plume in the air; another phenomenon that is not included in our model.

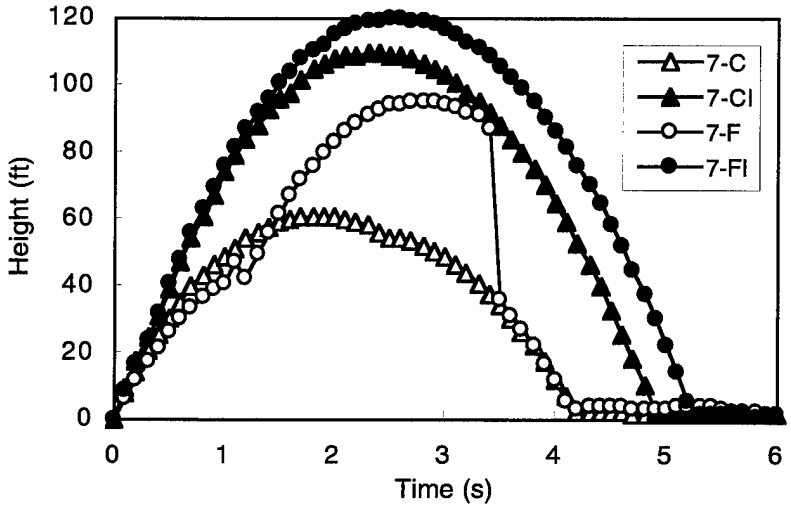

Fig. 3 — Computed plume heights for Shot 7

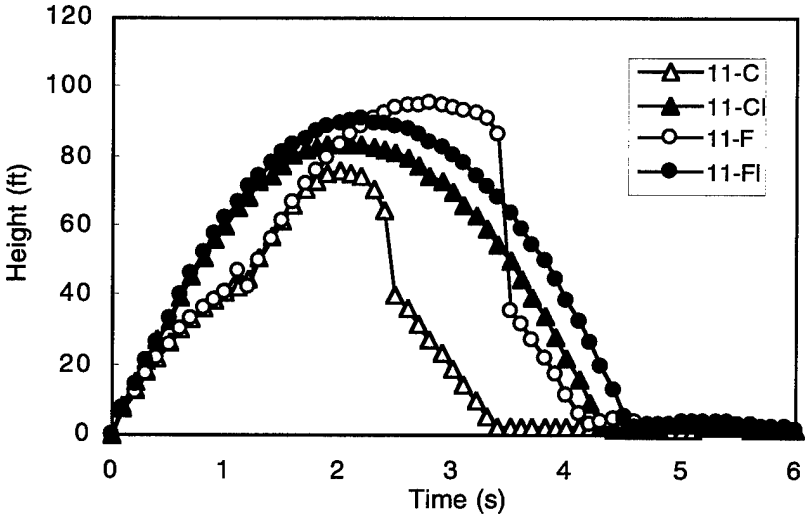

Fig. 4 — Computed plume heights for Shot 11

The results for the deeper case, Shot 11, are shown in Fig. 6. As before, the computation with the flat initial surface, Run 11-F, under predicts the measured values at all times, while Run 11-FI predicts heights below the measurements at early times and exceeding the measurements at later times.

We remark that the measured values used in Fig. 6 were not taken from Ref. 18. While our estimates from the video data agreed with their results for all other shot cases, our estimates for

Shot 11 were 25 to 30% higher. Since the digital images used in that report were not saved and hard copies of the video sequences were not printed, it was not possible to reproduce the measurements presented in Ref. 18. However, we attempt to justify our measurements by comparing pictures from the video sequence and computations for each shot.

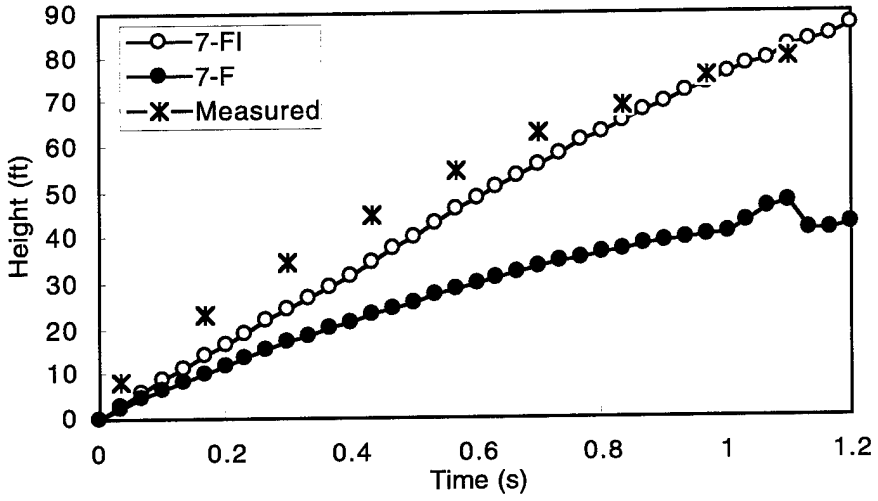

Fig. 5 — Computed and measured plume heights for Shot 7

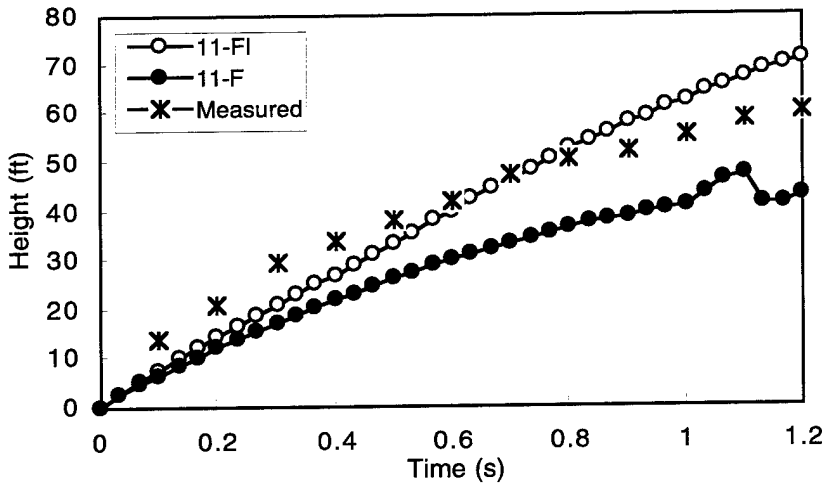

Fig. 6 — Computed and measured plume heights for Shot 11

Figure 7 shows a sequence of side-by-side comparisons of video frames from the experiment and computed density contours from Run 7-FI of the plume evolution for Shot 7. At early times, $t < 0.8$, the computations under predict the observed plume heights. This may be due to the water spalled upward due to the initial shock reflection. The outline of the numerical spray region appears to provide a rough approximation to the outline of the actual plume. The emergence of the secondary

plumes through the spray outline coincides at $t = 0.8$ in both the computation and the experiment. At later times, the secondary plume has a greater horizontal velocity and lower vertical velocity in the experiment than the computation indicates. Still, the overall qualitative agreement between the computation and experiment is remarkable, considering the complexity and duration of the phenomenon. The total duration of the plume above the water surface is slightly under predicted by the computations as indicated at $t = 5.0$. This can be expected due to the drag on the fine water droplets comprising the spray in the plume at the late times.

Figure 8 shows a sequence of side-by-side comparisons of the plume evolution for Shot 11. In this case the early time plume profiles are in better agreement for $t < 0.8$ than with Shot 7. Here, the numerical spray region more closely matches the opaque spray surrounding the plume. The secondary plume, which can be seen in the numerical spray region at $t = 0.8$, has not yet emerged from the spray outline, as it appears in the video frame. Also, as with Shot 7, the computed secondary plume rises higher than in the experiment. Since this secondary plume appears to be comprised primarily of spray, drag may be effecting its motion substantially. The overall duration of the plume above the surface is reproduced well by the computation, as indicated at $t = 4.4$.

Note the difference in scale of the video frames from the two shots as shown in Fig. 7 and Fig. 8. The grid marks in each case were based on matching measured plume heights at corresponding times from video frames taken at a 90° angle to the line charge. These latter frames had fiducials so that precise scale measurements could be made (see Ref. 18). As an additional check of the scale used in Figs. 7 and 8 observe the profile of the trees in the background. The field of view (FOV) for Shot 11 (Fig. 8) is obviously narrower than for Shot 7 (see Fig. 7). The grid scales used in these figures closely match the difference in the FOV. When this difference in the FOV is taken into account, the plume heights for Shot 11 agree with those presented in Fig. 6 but, as previously mentioned, are 25 to 30% higher than reported in Ref. 18.

Microwave Data

Measurements of the plume density using microwave measurements were first discussed in Ref. 20. These measurements were based on the amount of microwave absorption through the plume. Microwaves were sent and received using a pair of 3-ft radius parabolic dishes placed on either side of the plume at equal heights above the water surface. To compare the microwave measurement with the computed densities, the computed values were integrated within a cylindrical region of radius 3 ft, corresponding to the region between the parabolic dishes. At time t^n, this integral, representing the total amount of water between the dishes, can be expressed as

$$I(t^n, H, R, L) \equiv I^n(H, R, L) = \int_{H-R}^{H+R} dz \int_{-r(z)}^{r(z)} dy \int_{-L}^{L} \rho^n(x, y, z) dx \tag{29}$$

where $R = 3$ is the radius of the dishes, H is the height of the center of the dishes, $2L$ is the distance between the dishes, and

$$r(z) = \begin{cases} \sqrt{R^2 - (z-H)^2} & \text{if } |z-H| \le R \\ 0 & \text{otherwise} \end{cases}. \tag{30}$$

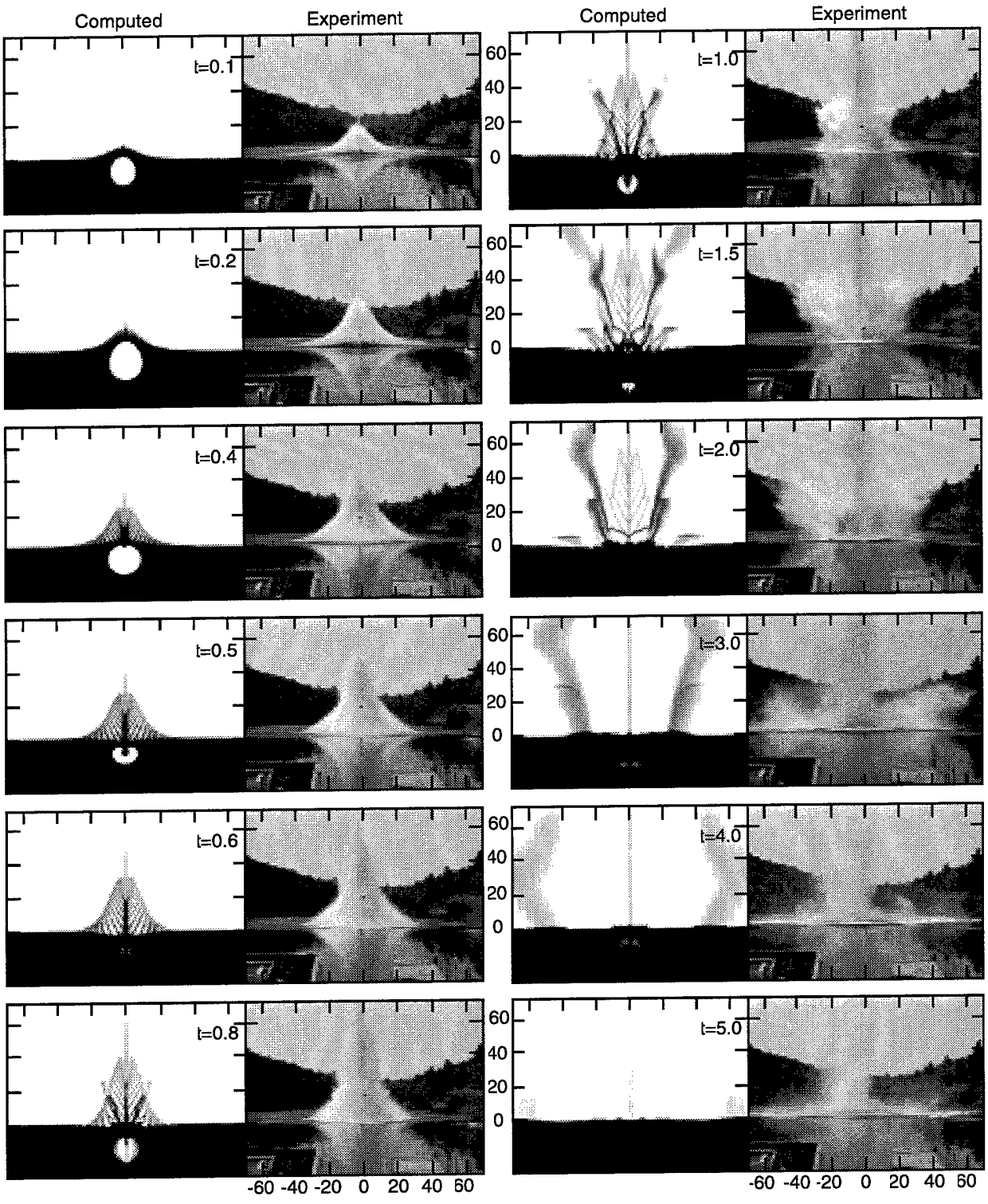

Fig. 7 — Video frames and computations for Shot 7

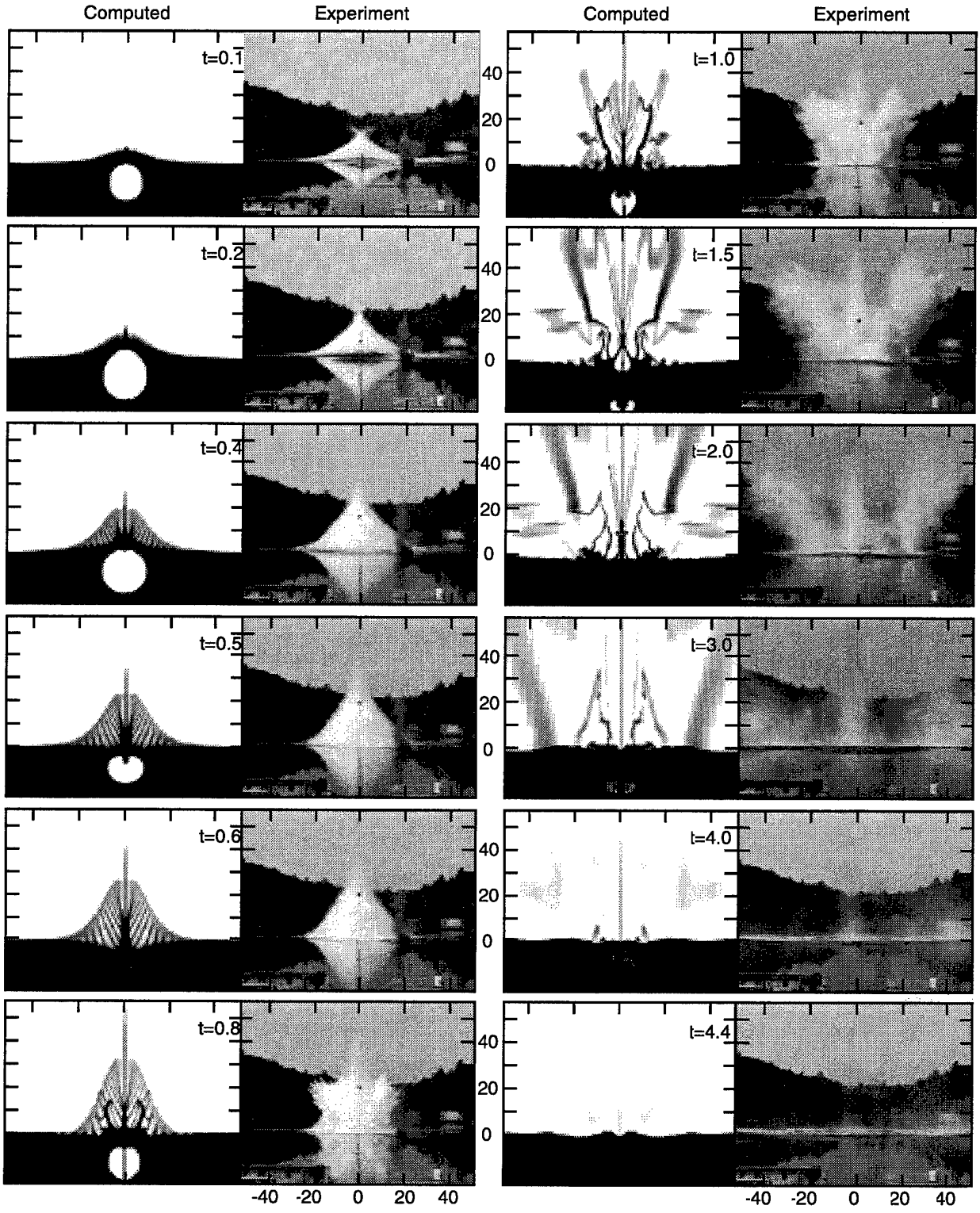

Fig. 8 — Video frames and computations for Shot 11

In both the experiment and the computations the value for L was sufficiently large to contain the entire width of the plume. For 2-D approximations, ρ^n does not change in the y direction (parallel to the line of charges and perpendicular to the line between the microwave dishes). Therefore, using symmetry across $x = 0$, it follows that

$$I^n(H,R,L) = 4\int_{H-R}^{H+R} r(z)\int_0^L \rho^n(x,y,z)\,dx\,dz. \tag{31}$$

This integral is approximated numerically using the quadrature formula

$$I^n(H,R,L) \approx I_h^n = 4\sum_{j=J_1}^{J_2} r(\tilde{z}_j)\sum_{i=1}^{N} \rho_{i,j}^n (\Delta x)_i (\Delta\tilde{z})_j, \tag{32}$$

where

$$\tilde{z}_j = \frac{z_j^T + z_j^B}{2}, \qquad (\Delta\tilde{z})_j = z_j^T - z_j^B, \qquad (\Delta x)_i = x_{i+1} - x_i,$$
$$z_j^T = \min(H+R, z_{j+1}), \qquad z_j^B = \max(H-R, z_j),$$
$$J_1 = \max\{j : z_j \le H-R\}, \qquad J_2 = \min\{j : z_j \ge H+R\}.$$

This mass is converted into an *equivalent water length* (*EWL*) by

$$W(t^n,H,R,L) \equiv W^n(H,R,L) = \frac{I^n(H,R,L)}{\rho_0 \pi R^2}, \tag{33}$$

corresponding to the length of water filling the cylinder having an equivalent mass as the plume intersected with the cylinder. The cylinder is horizontal with its axis at height H, with radius R, and length $2L$. (For the microwave data the length of the cylinder or distance between the dishes is not significant since this distance is much greater than the width of the plume. That is, W will not change if L is sufficiently large.)

Figure 9 shows the computed and measured microwave data for Shot 7. The measured values for this shot became saturated at a peak value of 1.56 as indicated by the flat plateau in its graph. The graph of the measured data begins rising approximately 0.15 s earlier than the computed results that corresponds to the plume height data presented in Fig. 5. Since the plume heights from the runs with the indented surface were in better agreement with the measurements, only data from those runs are presented here. At early times ($t < 0.8$), only the central plume passes through the microwave cylinder. Both computations appear to severely under predict the amount of water in the central plume at this height. Consider the structure of the computed plume at $t = 0.5$ in Fig. 2. The density contours indicate a thick wall of water rising to a height of about 20 ft. Above this thick region is a much thinner plume resulting from the initial indentation. According to the computations, the thick part of the plume begins to thin out before it reaches a height of 25 ft. Therefore, reducing H generally increases W. For example, Run 7-FI yielded $W(0.5,12.5,3.0,L) = 3.3$, compared to $W(0.5,25,3.0,L) < 0.5$, as indicated in Fig. 9. The peak in the computed values at approximately $t = 1.0$ occur as the secondary plumes pass through the microwave height. This peak is followed by a smaller peak as the water at the top of the secondary plume falls back downward. Since the secondary plume was not ejected upward as high in the coarse grid run, the smaller peak appears substantially

earlier ($t = 1.3$) for Run 7-CI than the time ($t = 2.1$) it appears for Run 7-FI. At later times ($t > 3$), the fine grid run and the measured data are in better agreement.

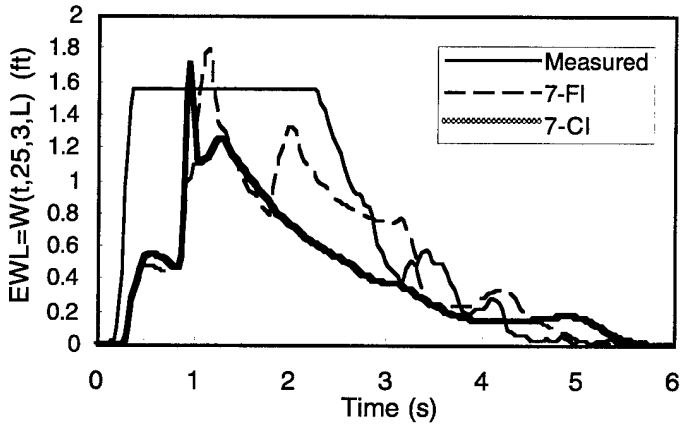

Fig. 9 — Computed and measured microwave data for Shot 7

Figure 10 displays the microwave results for Shot 11. Here the initial rise in the graphs for $t < 0.5$ are all in agreement. However, while the measured data rises and then falls (consistent with the peak computed plume heights shown in Fig. 4), the computed data for Run 11-FI peaks at $t = 1.0$ as the secondary plume rises above 25 ft (cf., Fig. 8). While the computed equivalent water length values range between 1.1 and 1.7 for $1 < t < 2.1$, the measured data range between 2.0 and 3.2 during the same time period.

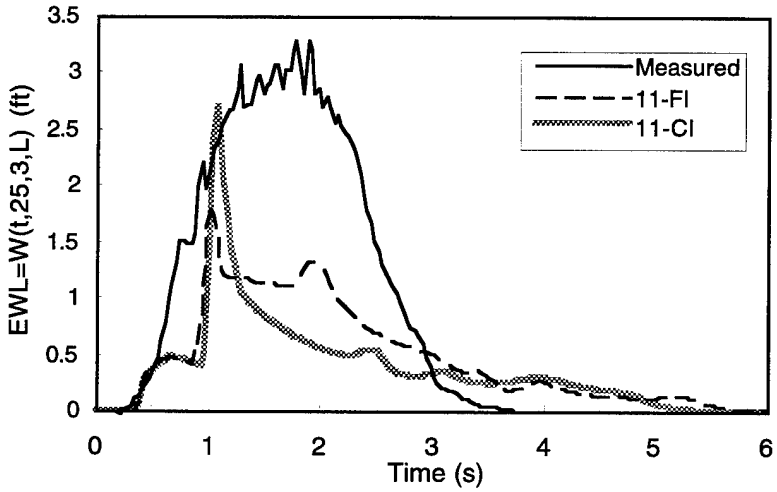

Fig. 10 — Computed and measured microwave data for Shot 11

Probe Data

In addition to the microwave data, plume densities were measured using conductivity probes. These probes were developed by Phillips and Scott [21] and consist of two parallel stainless steel rods whose conductivity is linearly proportional to its unwetted length. For these tests, fifteen probes

were suspended on a cable perpendicular to the line of charges at a nominal height of 12.5 ft. The use this technology for plume density measurements was conceived of and previously used by Lipton in Ref. 22. However, the measured height above the charges was only 11.5 ft as described in Ref. 23. The probes were spaced 1 foot apart with a central probe directly above the line of charges.

Making comparisons of density measurements at the individual locations is not meaningful due to the instabilities inherent in the plume formation. Indeed, there is very little agreement between probe pairs equally distant on either side of the charges. However, some success was achieved by making comparisons using an integral norm. As with the microwave comparisons, we define the effective water length W using (29) and (33), taking the limit as $R \to 0$. This yields

$$W(t,H,0,L) = \frac{1}{\rho_0} \int_{-L}^{L} \rho(t,x,y_p,H)dx, \tag{34}$$

where H is the height of the probe line, y_p the horizontal offset from the central charge (or center of the line charge), and $2L$ is the distance between the first and last probe in the line. Since the probes are located at discrete points, this quantity is approximated using the trapezoid rule quadrature

$$W_S = \frac{S}{\rho_0}\left[\rho_1/2 + \sum_{i=2}^{N-1}\rho_i + \rho_N/2\right], \tag{35}$$

where S is the uniform spacing between the N probes and ρ_i is the density at the ith probe location. The use of (36) with $S = 1$ and $N = 15$, corresponding to the actual probe locations, is referred to as "point line integration" (PLI). Later, we will also consider an approximation to Eq. (34) based on values for the densities inside each computational cell, with values for L greater than the plume widths. This will be referred to as "full line integration" (FLI).

The computational data was integrated at $H = 12.5$, as opposed to the 11.5 ft height of the cable. However, the cable was moved by the plume during the experiment so precisely that matching the height of the probe cable was not feasible. Figure 11 shows a comparison of the equivalent water lengths W_S, using Eq. (35) on the probe data and the computational data. While the peak values of W_S agree to within 15%, the peak of the computed values occurs at approximately $t = 0.5$ s, while the measured peak occurs at approximately $t = 1.2$ s. Compared to the microwave data, both the computed and measured probe data indicate much lower W values for $t > 2$. This is because after this time most of the plume has spread out beyond the 15 ft width straddled by the probes. Furthermore, the probes open downward and are not able to detect water falling downward due to a "shadowing" effect.

Figure 12 displays the comparison for Shot 11. Here, the computations are substantially higher than the measurements at almost all times. As the water in the plume is broken up into droplets and spray, the behavior of the probes is not well-known. In general droplets smaller than the width of the fork in the probes will not be detected. This may partially explain the large discrepancy in the data.

The integrity of all the data can be checked by comparing results from each measurement for one of the shots. Fig. 13 shows a comparison of the data for Shot 7 for $t < 1$. For $t < 0.8$, the plume is comprised of only the central water column, surrounded by spray from the initial shock reflection and Rayleigh-Taylor instability at the free surface. Therefore, it can be expected that the density probes span most of the water in the plume at these times. However, as seen in Fig. 13, the

integrated measured probe data is not only far below the computed data (Run 7-FI (PLI) and (FLI)), but it is also well below the measured microwave data recorded at over twice the height of the probe line. That the probes are spaced sufficiently close to resolve the plume structure and their 14-ft span is sufficiently wide during these times is supported by the similarity of the computational data using either point line integration at only the probe locations (PLI) or full line (FLI) integration at all cell locations. These two integration formulas begin to diverge after $t = 0.8$ as the wider secondary plume reaches the probe height. Another disturbing feature in Fig. 13 is that the microwave data, measured at 25 ft begins to rise at about the same time as the probe data, measured at 11.5 ft. These discrepancies suggest that inaccuracies in the measurements may be as significant as with the computations.

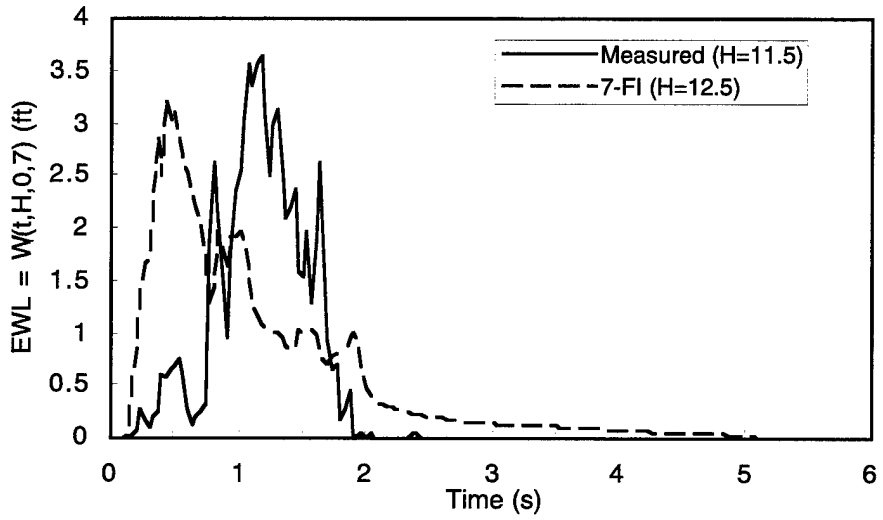

Fig. 11 — Computed and measured probe data for Shot 7

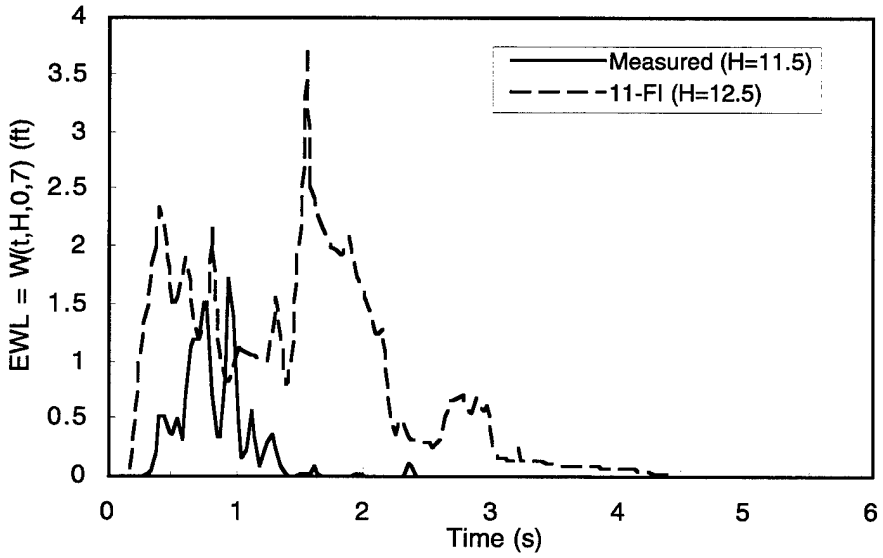

Fig. 12 — Computed and measured probe data for Shot 11

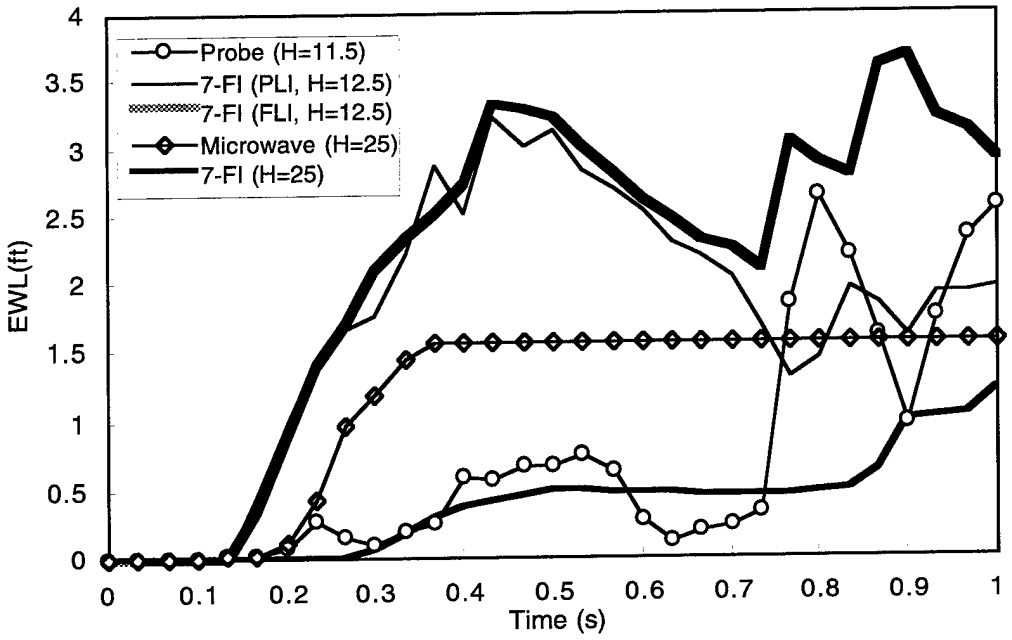

Fig. 13 — Early time density computations and measurements for Shot 7

Optimal Depth Study

Despite the relatively poor agreement between the computations, microwave data, and probe data, an optimality study, based on the computations, is presented. The validity of this study is based on the agreement in the measured plume heights and the qualitative agreement between the video frames and the computed density contours. The use of microwave and probe measurements has not been validated for plume density measurements independently. Therefore, even though the computations may (or may not) disagree with the actual plume water content at any individual charge depth, the dependence of the plume density on the charge depth may still be accurately predicted.

The computations were performed with initial charge depths between 1 and 21 ft. In particular runs were made at depths, $d = 1$, 1.5,...,4.5, 5.0, 5.2,...,9.8, 10.0, 11.0,...,15.0, 17.0, 19.0, and 21.0. The initial conditions used were the same as those based on the empirical laws described previously, modeling a line charge of $M = 1.25$ lbs/ft of C-4. Distances (including charge depths) may be nondimensionalized using the free-field maximum bubble radius. However, the effects of gravity do not scale, so the "nondimensionalized" results presented here can only be expected to be valid for charges producing bubble energies within an order of magnitude of these C-4 charges. Initially, the computations used an indented free surface with the radius of the indentation given by $R_I = 1.03d$, whenever the scaled depth is less than one, that is, $C = \dfrac{d}{A_{\max}^{(2D)}} \le 1$. As with the computations for Shot 7 and Shot 11, the runs were started on a grid that had a uniform fine grid region of cells with size $h_1 = 0.05$, surrounding the initial charge location. In all cases, the uniform region in the horizontal direction was restricted to the vertical strip, $0 \le x \le 2$. The uniform region in the vertical direction depended on the initial charge depth, as indicated in Table 3. In the cases when the top of the

uniform region was below $z=1$, cells of height $2h_1$ were added to extend the computational domain to $z=1$. As before, these initial grids were used for $0 \le t \le t_i = 0.007$, after which the solution was remapped onto the second grid. The uniform grid region for the second grid had cell size $h_2 = 0.4$, corresponding to the "coarse" grid used previously. The uniform grid region used for the second grid was the vertical strip $0 \le x \le 12$ intersected with the horizontal strip indicated in Table 3.

Table 3 — Uniform Grid Regions for Depth Dependence Runs

Depth Range	Initial Grid	Second Grid
$d<5$	$-7 \le z \le 1$	$-21 \le z \le 29$
$5 \le d \le 10$	$-12 \le z \le -3$	$-21 \le z \le 29$
$11 \le d \le 15$	$-17 \le z \le -9$	$-25 \le z \le 29$
$d>15$	$-d-2 \le z \le -d+2$	$-d-12 \le z \le 29$

In this study the expression "optimal" will refer to some functional $\boldsymbol{F}$ of the equivalent water length W as a function of the depth, d. Ideally, we seek d_{opt}, which satisfies

$$\boldsymbol{F}(W(t,H,R,L,d_{opt})) = \max_d \boldsymbol{F}(W(t,H,R,L,d)). \tag{36}$$

Two specific forms for $\boldsymbol{F}$ will be used. The first is simply the time integral of W, namely,

$$f_1(d,T) \equiv F_1(W(t,H_D,R_D,\infty,d),T) = \int_0^T W(t,H_D,R_D,\infty,d)dt, \tag{37}$$

which has units of *mass-time*. The second functional measures the length of time that W is greater than or equal to some threshold. More precisely,

$$f_2(d,E_W,T) \equiv F_2(W(t,H_D,R_D,\infty,d),E_W,T) = m(\{t : W(t,H_D,R_D,\infty,d) \ge E_W\} \cap \{0 \le t \le T\}), \tag{38}$$

where m refers to the Lebesgue measure (length) of the set. The threshold value E_W may relate to some predetermined value for which the plume makes an effective barrier.

Three choices for the pair (H, R) are (12.5, 0.5), (16.5, 5.5), and (25.0, 0.5). These will be referred to as *low*, *average*, and *high*, respectively. The "low" and "high" choices correspond to what would be encountered by a one-foot diameter missile at heights of 12.5 and 25 ft, respectively. The "average" represents a weighted average between heights 11 and 22 ft. This roughly corresponds to the scaled heights between 1 and 2 A_{max}.

A graph of the function $f_1(d,T)$ for the three choices of (H, R), is shown in Fig. 14 below, with $T = 6.0$ (the entire plume duration). Due to the oscillations in the computed data, an approximation of d_{opt} cannot be confidently determined. However, some of the features of these graphs become clearer after the data has been smoothed. The smoothing of the data was performed using $g_s = A^{10}(g)$, where $A(g)_i = (g_{i-1} + 4g_i + g_{i+1})/6$ and g is the vector of values of $f_1(d,T)$ interpolated (if necessary) to the uniform grid $d_i = 1 + 0.2i$ for $i = 0,...,100$. The values at the endpoints $i=0$ and $i=100$ are held fixed by the smoothing.

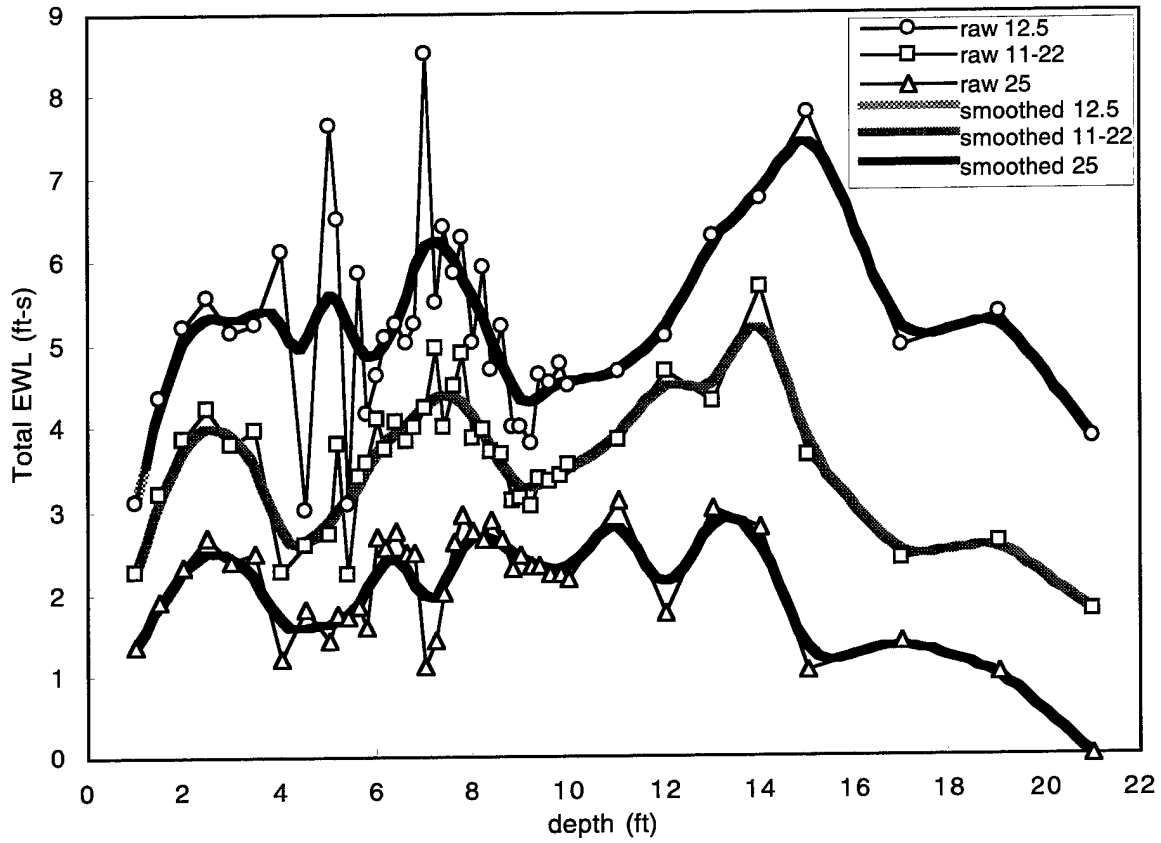

Fig. 14 — Smoothed and raw computed values for $f_1(d,T)$

A phenomenological argument explaining all of the relative extrema shown in the data cannot be made at this time. However, the three clear relative maxima, appearing in the "average" case, can be partially explained by a careful examination of the computed results. At shallow depths, $C < 0.5$ ($d < 6$), the bubble can be expected to vent before its first period (time of minimum volume). For very shallow depths ($d < 2.0$), the venting occurs early and the amount of water ejected upward is almost exactly proportional to amount initially above the bubble (charge). As the depth increases, the time of venting also increases. Eventually, venting will not occur until after the bubble attains a pressure below the ambient pressure. During this time, the water above the bubble is accelerated downward, thereby decreasing the amount ejected upwards. This explains the first relative maximum at $d = 2.5$ ($C = 0.21$). When venting is delayed until after the first bubble maximum volume, the velocities of the surrounding water point toward the bubble's center causing it to contract. A high pressure region forms above the bubble due to the water rushing inward in the relatively thin layer between the bubble and the air. This causes the formation of the central plume ((cf., Figs. 7 and 8) $t = 0.4$ and 0.5). Due to the relatively thin layer of water above the bubble at this time and Rayleigh-Taylor instability, some "fingering" of the free surface can pierce the bubble causing some venting to occur. The amount of water in the plume depends on how late venting occurs. At depths $d > 6.0$ ($C > 0.5$), the bubble no longer vents during its first pulse. As the depth increases, the central plume thickens but attains lower maximum heights. The second relative maxima in f_1 for the "average" choice occurs at approximately $d = 7.6$, ($C = 0.66$). Adding to the total water ejected are the secondary plumes that appear during the bubble's second expansion (cf., Figs. 7 and 8, $t = 0.8$). While the total amount of water in the central plume appears to diminish after $d > 8.0$, the amounts ejected

by the secondary and tertiary pulses increase, and the global maximum appears at $d = 14.0$, ($C = 1.3$) for the "average" choice. At the "low" height, the global maximum occurs at $d = 15$ and, at the "high" height, it occurs at the shallower depth of $d = 13$. This can be explained by tertiary plumes contributing more water and rising to maximum heights between 12.5 and 22 ft.

The theory described above is also supported by the graph of the smoothed second functional f_2 defined by Eq. (38). Figures 15 and 16 display graphs of $f_2(d,1.5,6.0)$and $f_2(d,1.5,2.0)$, respectively. The similarity in these two sets of graphs for $d < 10$ demonstrates that for these depths most of the water appears in the plumes for the first 2 s after the detonation. However, for $d > 12$, a substantial amount of water is ejected upward after 2 s. This corresponds to times after several bubble pulses have occurred. The relative maximum at $d = 18.8$ at the "low" height for $f_2(d,1.5,6.0)$ is almost twice its corresponding value for $f_2(d,1.5,2.0)$. This indicates that, for depths near $d = 19$, a plume rising just above 12.5 ft is ejected upward shortly before $t = 2$ and contains a substantial amount of water.

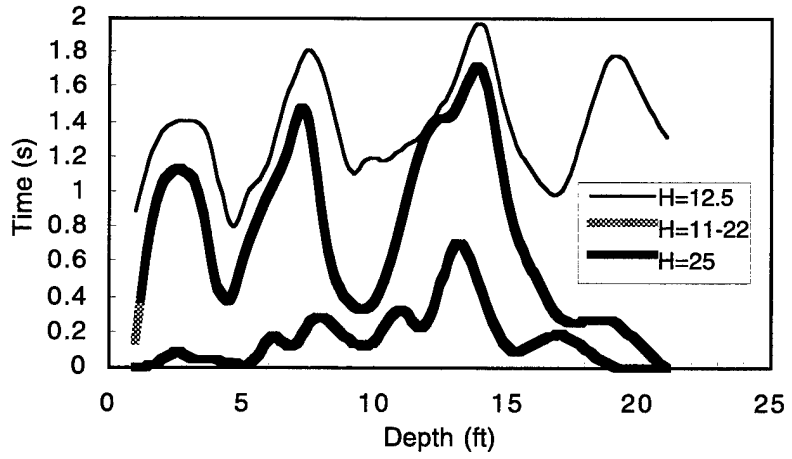

Fig. 15 — Smoothed computed values for $f_2(d,1.5,6.0)$

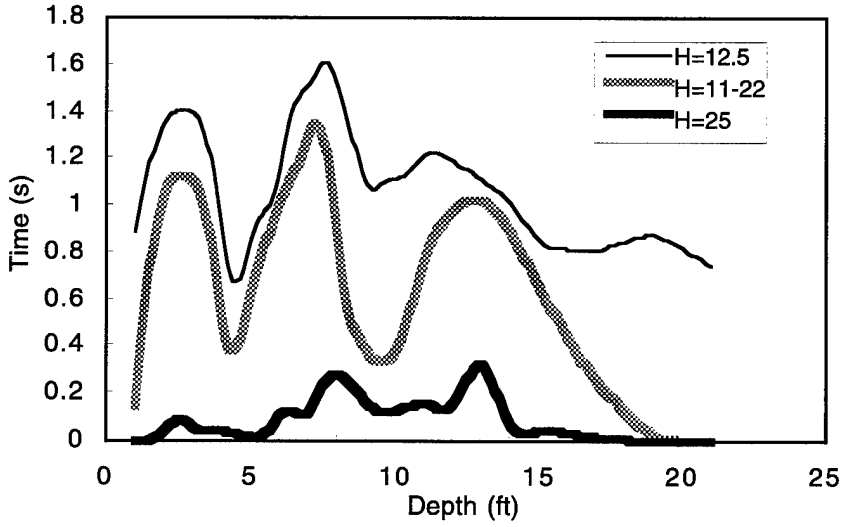

Fig. 16 — Smoothed computed values for $f_2(d,1.5,2.0)$

Validations of the Three-Dimensional Model

The BUB3D code was used to model the effects of using discrete charges as opposed to the continuous line charge approximated with the 2-D model. The goal of this computational experiment was to predict the difference in the plume structure observed between the use of discrete or continuous line charges. This difference is conjectured to be caused from shock interactions at the free surface between the discrete charges shortly after a (nearly) simultaneous detonation. The incompressible liquid model was initialized using the empirical shock model depicted in Fig. 1. In particular, the choices $R_I = 1.03d$ and $R_F = 1.1\sqrt{d^2 + (S/2)^2}$ were used to initialize the density.

The assumption that the line charge is of infinite extent was retained from the 2-D model, so that only one variable (initial charge shape) was changed. This approximation was implemented, using an extra symmetry plane, centered between two discrete charges. A second symmetry plane, parallel to the first and cutting through the center of the initial charge location, was also used. Finally, the model includes a third symmetry plane, containing the line of charges. This third plane corresponds to the symmetry plane used in the two dimensional computations. If an initial charge is located at coordinates $(x, y, z) = (0, 0, -d)$ and the initial standoff distance between the charges is S, then the three symmetry planes described above are located at $y = S/2$, $y = 0$, and $x = 0$, respectively.

Using the conditions for Shots 2, 6, and 9, namely, $d = 8.2$, $W = 10$ lbs of Composition C-4, it follows from Eqs. (18-23) that $A_{\min} = 0.61617$, $A_{\max} = 9.3$, and $p_B^0 = 1535.7P_\infty$. (Note, this is the same initial pressure as for the 2-D model for Shot 7.) As with the 2-D model, a two-grid solution procedure was used. The initial grid contained a fine uniform region of cell "cubes" of size $h_1 = 0.1$ in the region $0 \le x \le 2$, intersected with $0 \le y \le 4$ and $-10.2 \le z \le -6.2$. Above this region the cells were stretched vertically to a maximum size of $h_z = 0.2$, using 46 cells, extending the domain to $z = 2.0$. The grid was stretched downward to $z = -50$, using an additional 12 cells. In the x-direction, cells were stretched to $x = 50$, using an additional 10 cells. Overall, the initial grid was comprised of $30 \times 40 \times 98$ cells.

The second grid had a resolution corresponding to the "coarse" grids used in the 2-D study. The uniform region was composed of cubic cells of size $h_2 = 0.4$ in the region $0 \le x \le 12$ intersected with $0 \le y \le 4$ and $-20 \le z \le 30$. Additional stretched cells extended the domain down to $z = -100$, up to $z = 150$, and across to $x = 100$. The second grid used a total of $50 \times 10 \times 185$ cells.

Figure 17 shows a composite of video images from Shot 6 and the 3-D computations. The view displayed in these images is the "front" view, perpendicular to the line of charges and the images shown in Figs. 7 and 8. Density plots from the computations overlay the video images in the range $0 \le y \le 28$. These plots were created by reflecting and copying plots from the actual computational region $(0 \le y \le 4)$ by symmetry.

The video image at time $t = 0$ corresponds to a time shortly after the charge detonations. The density plot overlaying this image corresponds to the computation at $t = 0.0035$, the initial time for the remapped solution on the second grid. At this time the bubbles are still discrete and nearly spherical. The indentations at $z = 0$ for the empirical model of the shock interactions can be observed. The shock interactions may be clearly observed as white "bumps" above the line of charges at the midpoints between the charges. Curved white lines emanating from these points on either side of the charge line are also observable in this image. The curve in these lines is due to slightly asynchronous detonation (from right to left) of the charges. At $t = 0.1$, seven distinct "finger

plumes" can be seen rising to a height of about 20 ft, compared to 15 ft in the computations. The computed shorter plumes directly above the initial charge locations arise from the initial indentation of radius R_i. In the video it is difficult to see this detail in the plume structure. The computed bubble is now cylindrical shaped separated by a thin membrane at the symmetry wall. The bubble expands attaining a maximum volume at $t = 0.266$, and the contraction can be clearly observed at $t = 0.4$. The bubble continues its collapse until shortly after $t = 0.5$. The height of the plume fingers is under predicted by the computations for $t < 0.3$ and slightly over predicted for $t > 0.3$. At the later times, the plume velocity can be expected to be influenced by air resistance. Air resistance is not modeled in the computations. This is a likely cause of the over production of the plume heights for $t > 0.3$.

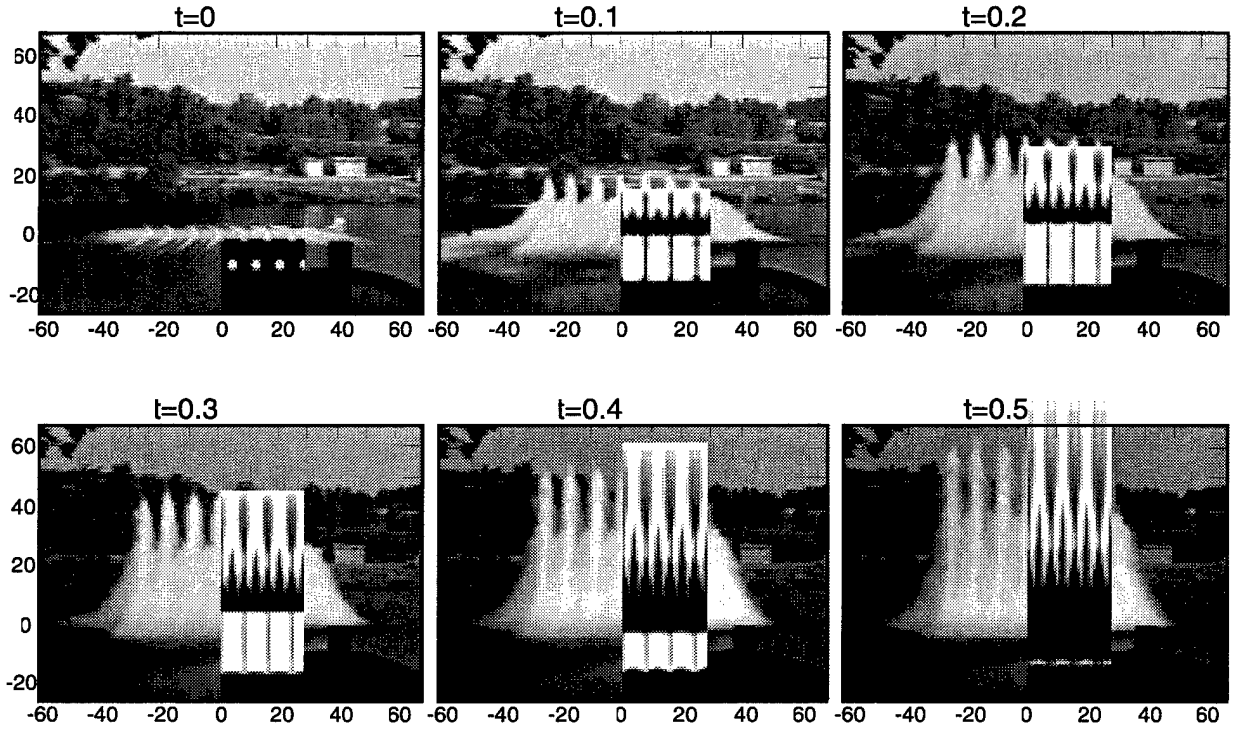

Fig. 17 — Composite of video images and computed density plots for Shot 6

A comparison of the measured and computed plume heights is shown in Fig. 18. Also included were measured plume heights from Shots 2 and 9 (same depth and standoff as Shot 6 but using only 5 charges). The plume heights from Shots 2 and 9 are slightly lower than for Shot 6, and they are in better agreement with the computation for $t < 0.3$ and in worse agreement for $t > 0.3$.

Figure 19 displays perspective images of the 3-D computation. In these frames, two isocontours of density are displayed. For the plume above z = 0, the isosurface $\rho = 0.001\rho_0$ is rendered in light gray, while for the bubble below z = 0 the isosurface $\rho = 0.5\rho_0$ is rendered in dark gray. At $t = 0.2$, the bubble is clearly seen to be cylindrical in shape. A 2-D jet can be seen piercing the top of the cylindrical bubble at the start of the collapse phase at $t = 0.4$. The ejection of the secondary plumes can be seen at times $t = 1.0$ and $t = 1.2$. These secondary plumes appear later in this calculation than in the analogous 2-D computation (cf., Fig. 7) due to the bubble venting into the air region during its collapse. When the bubble reformed it continued to collapse but had less energy for the second expansion.

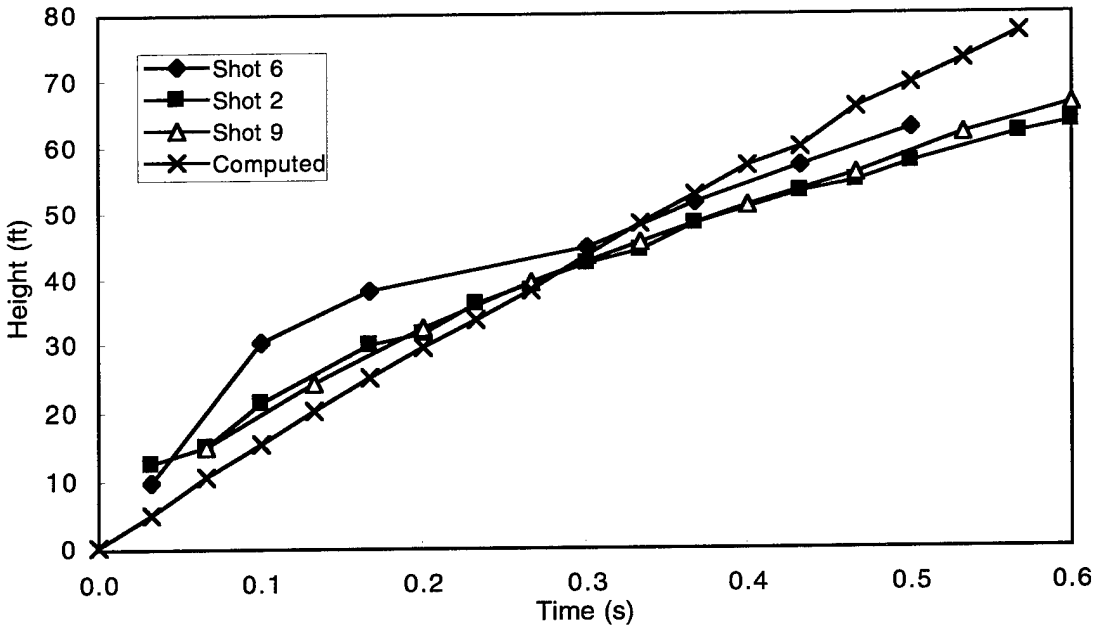

Fig. 18 — Computed and measured plume heights for discrete charge shots

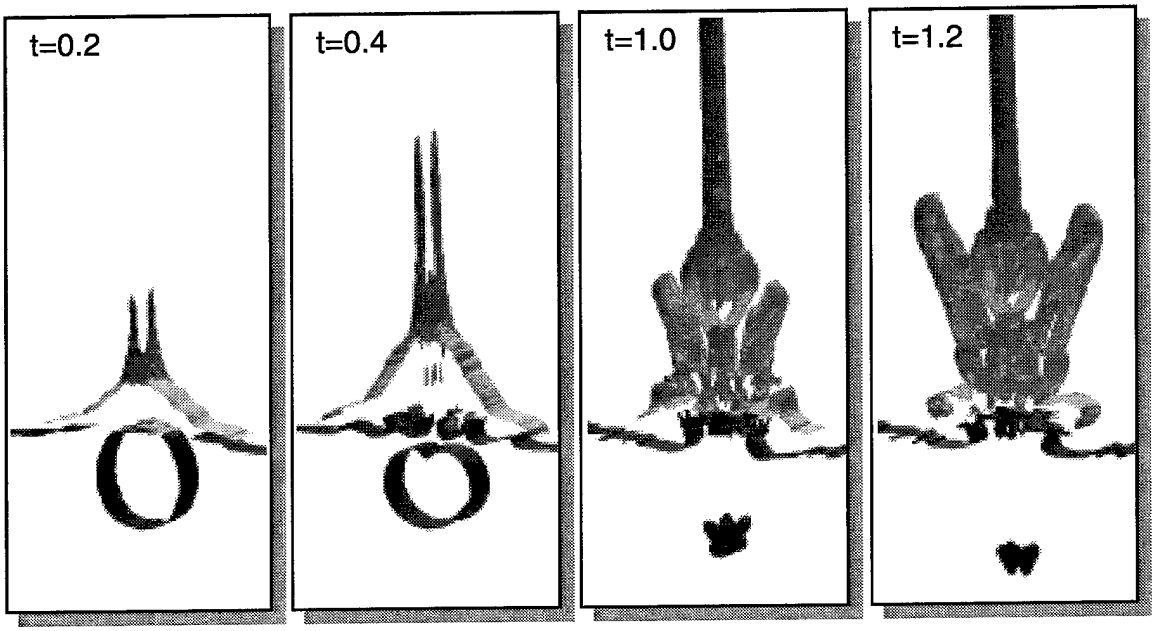

Fig. 19 — Computed bubble and plume isocontours for Shot 6

SUMMARY AND CONCLUSIONS

This report presented comparisons between computational and experimental measurements of plumes produced by underwater explosions. Of particular interest was the study of charge configurations, which create a plume "barrier" by ejecting a "wall of water" above the surface. Such an effect occurs after either the nearly simultaneous detonation of discrete charges placed sufficiently close together in a line, or the detonation of a continuous line of charges.

The overall hydrodynamic phenomena involved in this process is extremely complicated. The bubble formed from underwater detonation can undergo several cycles or periods before it vents. During each cycle, hydrodynamic instabilities can be expected at both the bubble-water and air-water interfaces. Rayleigh-Taylor instabilities occur whenever a denser material (water) is accelerated into a less dense material (bubble gas, or air). These instabilities occur at the bubble interface when the bubble is near its minimum volume and the bubble pressure is above the ambient hydrostatic pressure. They also occur at the air-water interface as the bubble begins its contraction. Such instabilities make pointwise density comparisons meaningless. Combined with the long-time behavior of the overall dynamics, the numerical accuracy of the computations is also an issue. Nevertheless, the overall dynamics of the plume formation and secondary plume ejection is reproducible experimentally, and as was demonstrated in this paper, computationally as well.

Numerical accuracy of the computations was studied by comparing the predicted dynamics using two different grids (fine and coarse), with sizes differing by a factor of two. For relatively early times ($t < 1.0$) the differences in the solutions were very small (cf., Fig. 2) but became more apparent at later times. These differences were also studied quantitatively by comparing computed plume heights (cf., Figs. 3 and 4). Comparisons were made with and without an indented free surface used to empirically model the shock effects.

The use of an empirical model (cf., Fig. 1) for shock effects at the air-water surface was found to be critical for accurate predictions of the plume heights. For continuous line charges, the model accounts for the reflection of the cylindrical shock off the air-water interface by initializing the interface with a small channel in the water directly above the line charge. When this model was used, the predicted plume heights were initially lower than those observed (for $t < 0.3$) probably due to water spalled upward from the shock reflection unaccounted for in the model. At later times the computed plume heights eventually exceed the observed heights (cf., Figs. 5 and 6). This over prediction is conjectured to be caused by the lack of air resistance in the computational model.

By also including the effects of shock interaction between discrete charges, the plume heights for a discrete line charge case accurately matched the observed heights using a 3-D computational model (see Fig. 18). In the discrete charge case, the plume heights are generally higher than with an equivalent line charge due to the "fingering" of the plumes between the charge locations. This fingering effect was reproduced by the 3-D computation using the empirical shock model (see Fig. 17).

Secondary plumes are ejected (for scaled charge depths $C > 0.5$) for line charges and single discrete charges. For discrete charges, secondary (radial) plumes were first accurately predicted in Ref. 2. For continuous line charges, the emergence of secondary plumes has been observed and accurately predicted in this study (see Figs. 7 and 8). These secondary plumes were also predicted using the 3-D model (see Fig. 19). This computation also demonstrated the cylindrical shape of the merged bubbles during their first expansion.

Comparisons of computed and measured plume densities were unfortunately less successful. The computations predicted significantly less density in the plume than the amounts determined using the microwave absorption measurements (see Figs. 9 and 10). However, the computations predicted either more (see Fig. 12) or roughly the same (see Fig. 11) total amount of water in the plume as determined by the conductivity probe measurements. The disagreement of the measured results, due to the measurement techniques and the lack of calibration, undermines their use as a validation tool for the computations.

The optimal depth study was complicated by the relative unsmoothness of the results as a function of depth (cf., Fig. 14). Even when the results were regularized, several relative maxima appeared. Furthermore, the results were dependent on both the measure used and the height at which the densities were integrated. For the range of depths studied ($0.1 < C < 2.2$), three relative maxima appeared consistently for all the cases considered. Conjectures were made to explain these relative maxima but were not verified by either additional computational or experimental tests.

Improvements in the predictive model can be made in several ways. One improvement would be to eliminate the empirical conditions used for the initial conditions, using a validated code which includes compressible effects for the water region. The compressible code would need to be run for only a relatively short duration until the shock and reflected rarefaction wave are sufficiently far from the initial charge location. After this time, the results of the compressible code could be used as initial data for the currently used BUB2D or BUB3D codes. Another relatively straightforward improvement would be the inclusion of a model for the "air". In the current model, the air is simply a void with uniform density. Treating the air as a second incompressible species, with a prescribed density, may yield more accurate late-time plume feature predictions.

ACKNOWLEDGMENTS

The research in this report related to the Water Barrier Ship Self Defense Concept was supported by D. Siegal, ONR, Code 351. The basic research required for the development of the computational method and some of the theory presented was supported, in part, by R. Lau, ONR, Code 311, and the NSWC Independent Research Fund.

In addition to the sponsors of this research, the authors would like to acknowledge the work of J. Connor, Epoch Engineering, Inc., for operating the video equipment and providing plume height measurements profiles; K. Boulais, J. Choe, and K. Erwin, NSWCDD B42, for providing the microwave data measurements; and L. Lipton, NSWCIH 450, for providing the density probe data.

REFERENCES

1. C.E. Higdon, "Water Barrier Ship Self-Defense Concept," NSWCDD/MP-94/94, Naval Surface Warfare Center, Dahlgren Division, Dahlgren, Va., 1994, pp. 140-153.

2. W.G. Szymczak and J.M. Solomon, "Computations and Experiments of Shallow Depth Explosion Plumes," NSWCDD/TR-94/156, Naval Surface Warfare Center, Dahlgren Division, Dahlgren, Va., 1996.

3. R.H. Cole, *Underwater Explosions* (Princeton University Press, Princeton, N.J., 1948) Ch. 8, pp. 270-353.

4. J.C.W. Rogers, W.G. Szymczak, A.E. Berger and J.M. Solomon, "Numerical Solution of Hydrodynamic Free Boundary Problems," in *Free Boundary Problems, International Series of Numerical Mathematics,* (Birkhäuser Publishing Ltd., Basel, Switzerland, 1990), **95,** pp. 241-266; Proceedings of the Conference on Free Boundary Problems—Numerical Methods and Optimal Control, K.-H. Hoffmann and J. Sprekels, eds., July 9-19, 1989, Oberwolfach, Germany.

5. W.G. Szymczak, J.M. Solomon, A.E. Berger, and J.C.W. Rogers, "A Numerical Method Based on a Generalized Formulation of Hydrodynamic Free Surface Problems," Proceedings of the AIAA 10th Computational Fluid Dynamics Conference, June 24-27, 1991, Honolulu, Hawaii, AIAA-91-1541-CP, June 1991, pp. 155-165.

6. W.G. Szymczak, J.C.W. Rogers, J.M. Solomon, and A.E. Berger, "A Numerical Algorithm for Hydrodynamic Free Boundary Problems," *J. Comp. Phys.* **106**, 319-336 (1993).

7. W.G. Szymczak, "Energy Losses in Non-Classical Free Surface Flows," in *Bubble Dynamics and Interface Phenomena, Fluid Mechanics and its Applications* (Kluwer Academic Publishers, Dordrecht, The Netherlands, 1994), **23**, pp. 413-420; Proceedings of an IUTAM Symposium, J.R. Blake, J.M. Boulton-Stone, and N.H. Thomas, eds., Sept. 6-9, 1993, Birmingham, U.K.

8. W.G. Szymczak, J.C.W. Rogers, J.M. Solomon, and A.E. Berger, "Numerical Simulations of Cavitation Inception," Proceedings of CAV '95, The International Symposium on Cavitation, May 2-5, 1995, Deauville, France, 1995, pp. 399-406.

9. J.C.W. Rogers and W.G. Szymczak, "Computations of Violent Surface Motions: Comparisons with Theory and Experiment," *Phil. Trans. R. Soc. Lond.* **355**(A), 649-663 (1997).

10. W.G. Szymczak, "Computations and Experiments of Pressure Loadings from Underwater Explosion Bubbles," Proceedings of the 1997 ASME Pressure Vessels and Piping Conference, Y.S. Shin, ed., July 27-31, 1997, Orlando, FL., in *Structures Under Extreme Loading Conditions* (ASME, New York, 1997) **PVP-351**, pp. 17-27.

11. C.W. Hirt and B.D. Nichols, "Volume of Fluid (VOF) Method for the Dynamics of Free Boundaries," *J. Comp. Phys.* **39**, 201-225 (1981).

12. D.E. Kothe and R.C. Mjolsness, "RIPPLE: A New Model for Incompressible Flows with Free Surfaces," *AIAA J.* **30**, 2694-2700 (1992).

13. S.F. Davis, "Simplified Second Order Godunov-Type Methods," *SIAM J. Sci. Stat. Comput.* **9**, 445-473 (1988).

14. A.S. Almgren, J.B. Bell, and W.G. Szymczak, "A Numerical Method for the Incompressible Navier-Stokes Equations Based on an Approximate Projection," *SIAM J. Sci. Stat. Comput.* **17**, 358-369 (1996).

15. H.G. Snay, J.F. Goertner, and R.S. Price, "Small Scale Experiments to Determine Migration of Explosion Gas Globes Towards Submarines," NAVORD Report 2280, Naval Ordnance Laboratory, Silver Spring, Md., 1952.

16. M.J. Swisdak, Jr., "Explosion Effects and Properties: Part II—Explosion Effects in Water," NSWC/WOL TR 76-116, Naval Surface Weapons Center, White Oak Laboratory, Silver Spring, Md., 1978.

17. V.K. Kedrinskii, "Surface Effects from an Underwater Explosion (Review)," *J. Appl. Mech. and Tech. Phys.* **19**(4), 474-491 (1979).

18. J.G. Connor and C.E. Higdon, "Water Barrier Line Charge Plume Video Analysis," NSCWDD/TR-96/178, Naval Surface Warfare Center, Dahlgren Division, Dahlgren, Va., 1996.

19. J.R. Blake, B.B. Taib, and G. Doherty, "Transient Cavities near Boundaries. Part 1. Rigid Boundary," *J. Fluid Mech.* **170**, 479-497 (1986).

20. J.T. Choe, K.A. Boulais, K.A. Chun, and K.A. Irwin, "Microwave Probe for Mass Measurements of a Water Plume," NSWCDD/TR-95/187, Naval Surface Warfare Center, Dahlgren Division, Dahlgren, Va., 1995.

21. D.E. Phillips and B.W. Scott, "Development of Probes for Measuring the Maximum Radius of Underwater Explosion Bubbles," NOLTR 65-176, Naval Ordnance Laboratory, Silver Spring, Md., 1965.

22. L. Lipton, "Probe Measurement of Water Mass of Plumes Produced by Underwater Detonations," IHTR 1757, Naval Surface Warfare Center, Indian Head Division, Indian Head, Md., 1995.

23. C.E. Higdon, "Water Barrier Line Charge Plume Analysis," NSWCDD/TR-97/210, Naval Surface Warfare Center, Dahlgren Division, Dahlgren, Va., 1997.